JOURNAL OF GEOPHYSICAL RESEARCH, VOL. ???, XXXX, DOI:10.1029/,

Coherent pan–Asian climatic and isotopic response to orbital forcing of tropical insolation

D.S. Battisti,[1] Qinghua Ding,[1] and G.H. Roe[2]

Corresponding author: David S. Battisti, Dept. of Atmospheric Sciences,University of Washington, Seattle WA 98195-1640. (battisti@washington.edu)

[1]Dept. of Atmospheric Sciences,University of Washington, Seattle WA 98195-1640

[2]Dept. of Earth and Planetary Science,University of Washington, Seattle WA 98195-1310

Abstract. The oxygen-18 isotope composition of calcite in stalagmites across southern and eastern Asia are highly correlated to one another on orbital time scales: large negative excursions are coincident with maxima in summer insolation in the subtropics of the northern hemisphere (NH). These isotopic excursions reflect changes in the precipitation-weighted isotopic composition of precipitation, $\delta^{18}O_p$. We present results from two core experiments using an isotope-enabled climate model – the"high insolation" and "low insolation" experiments – in which the model is forced by extrema in NH summer insolation. Compared to the low-insolation experiment, the high-insolation climate features profound, large-scale changes in the pattern of monsoon precipitation spanning from Africa to Southeast Asia that are due to changes in the relative contributions of temperature and moisture to the near-surface equivalent potential temperature θ_e. Under high insolation, a more rapid increase in land surface temperature in early summer causes the greatest θ_e (and hence precipitation) to shift from the oceans in low insolation (such as today) to be over land in high insolation (such as the early Holocene). The model captures the general pattern of isotopic excursions seen in caves spanning from Israel to western China, including large drops in $\delta^{18}O_p$ over eastern Tibet (-7‰), the Arabian Peninsula and northeast Africa (-4‰). Although there are large changes in precipitation over Tibet, the change in $\delta^{18}O_p$ is due to changes in the $\delta^{18}O$ of water vapor that is delivered and subsequently precipitated; it does not inform on local precipitation amount or intensity.

1. Introduction

There have been remarkable improvements in the proxy records of climate from speleothems – in particular, the oxygen isotope composition of calcite in stalagmites, hereafter $\delta^{18}O_c$. The development of techniques for accurate, high-resolution dating based on the radioactive decay of uranium to its daughter products affords exceptional chronological control approaching an accuracy of 500 years per 100,000 years [e.g., *Cheng et al.*, 2012]. By patching together records from numerous samples from a single cave that are well-dated, numerous proxy records of the $\delta^{18}O_c$ have been constructed that span hundreds of thousands of years, albeit with gaps. The exceptionally accurate chronology, combined with the length of these speleothem records allow an unprecedented window of how the climate has changed on millennial and longer time scales.

Here we focus on the climate response to insolation forcing for several reasons. First, numerous long records are available across Asia and South America to reasonably define the amplitude of insolation-forced response in the speleothems. Second, these records show a coherent pan-Asian signal in $\delta^{18}O_c$ on orbital time scales, and have an amplitude (2 to 7 ‰) that is two or three times that associated with millennial scale changes in $\delta^{18}O_c$ (1 to 2 ‰), and two to seven times that associated with the interannual variability of the (precipitation weighted) isotopic composition of precipitation (1 ‰) [*Dayem et al.*, 2010].

The $\delta^{18}O_c$ in stalagmites from caves that meet certain criteria [*Schwarcz*, 2007] reflects the isotopic composition of water from which the calcite forms. Since the source of this water is ultimately precipitation that slowly percolates through the soil to the cave site, the $\delta^{18}O_c$ in speleothems can be directly related to the climatological oxygen isotopic composition of precipitation:

$$\delta^{18}O \equiv \left\{ {C_s}^{-1} \frac{^{18}O}{^{16}O} - 1 \right\} \times 1000, \tag{1}$$

where ^{18}O and ^{16}O are the amount of isotopes of oxygen delivered by precipitation over a time interval that is equal to or greater than the time it takes for the water to percolate from the surface to the cave site and the calcite to form. C_s is value of the Vienna Standard Mean Ocean Water (SMOW): 2.00520×10^{-3}. We can approximate Equation 1 by

$$\delta^{18}O \cong \frac{\sum_m \delta^{18}O_m \cdot P_m}{\sum_m P_m} \equiv \delta^{18}O_p, \tag{2}$$

where $\delta^{18}O_m$ is the $\delta^{18}O$ for the month m (i.e., Equation 1 applied to month m) and P_m is the total precipitation for month m. $\delta^{18}O_p$ is defined as the precipitation-weighted $\delta^{18}O$ of precipitation; to within $\mathcal{O}(C_s) \approx 0.2\%$, $\delta^{18}O_p$ is an accurate approximation to the climatological $\delta^{18}O$, equation 1 (see Appendix A). $\delta^{18}O_p$ will prove to be useful for illuminating the relative importance of changes in the seasonality of precipitation and changes in the isotopic composition of precipitation to the changes in the climatological $\delta^{18}O$ and in the speleothem $\delta^{18}O_c$.

We show in Figure 1 the time history of $\delta^{18}O_c$ from speleothems available from Asia that are sufficiently long to resolve orbital time scales. These records are (from top to bottom) from Hulu and Sanbao caves in eastern and central China, Tianmen Cave in Tibet, Kesang Cave in northwestern China, and Soreq and Peqiin Caves in Israel[1]; details on the location and source for each cave record are provided in Section 2.1 and Table 1. Superposed on each record is the June-August (JJA) insolation at 30°N. It is evident in Figure 1 that the $\delta^{18}O_c$ in these stalagmites is strongly forced by insolation – lighter (more negative) values of $\delta^{18}O_c$ are associated with greater insolation in the northern hemisphere (NH) summer. Evident in Figure 1 is a $\sim$20 kyr pacing of the cycles; this implicates a strong seasonal control on $\delta^{18}O_c$, predominately associated with climatic precession.

One measure of the fit is the correlation between insolation and the $\delta^{18}O_c$, the latter being interpolated to a regular (1000 year) increment. The correlations range from -0.37 at Soreq/Peqiin to -0.75 at Kesang; taking into account the auto correlation in the interpolated data, correlations are statistically different from zero at $p < 0.05$ for all records except Sofular in Turkey. Finally, the $\delta^{18}O_c$ from stalagmites in Hoti cave in Oman and Mukalla Cave in Yemen is also strongly paced by insolation forcing; in these cases, however, there is sufficient precipitation to grow stalagmites only during high NH summer insolation. Hence a correlation coefficient between the $\delta^{18}O_c$ from these caves and insolation is not informative.

Equally remarkable is the amplitude of this orbitally-driven signal. To make a rough estimate, we linearly regressed $\delta^{18}O_c$ against insolation. Since not all of the cave records are continuous, to make a direct comparison, we then multiplied the regression coefficient for each record by the difference in JJA insolation, 218 kbp minus 207 kbp: the high and low extrema in JJA insolation over the past 950,000 years. The results are summarized in Table 1. The peak-to-peak amplitude ranges from 1.6 ‰ in Israel to 7 ‰ in Tianmen. At Hoti and Mukalla, the $\delta^{18}O_c$ in the stalagmites that form during high NH summer insolation is at least 4 ‰ lighter than the $\delta^{18}O_p$ measured in precipitation today. The full range in amplitude at Tianmen, Hoti and Mukalla is uncertain because the speleothems do not grow during periods of low (Tianmen) or even moderate (Hoti and Mukalla) summer insolation. The $\delta^{18}O_c$ in Sofular cave in Turkey [*Fleitmann et al.*, 2009] is uncorrelated with insolation and tracks ice volume over the past 50 kyr; we will revisit this record and the Hoti and Mukalla records in Section 5.2.

In summary, the speleothem records paint a picture of orbitally paced changes in $\delta^{18}O_c$ that in turn suggest changes in the hydrologic cycle that are remarkable in both extent ($>$ 8000km) and amplitude ($>$ 7 ‰). As a reference point, the typical de-correlation length scale associated with interannual precipitation anomalies in the modern climate is typically $<$ 500km, and the amplitude of the $\delta^{18}O_p$ anomalies is typically $<$ 1‰ (see, e.g. *Dayem et al.* [2010]).

Although speleothem $\delta^{18}O_c$ is a direct measure of $\delta^{18}O_p$, $\delta^{18}O_p$ by itself cannot be directly or uniquely used to infer changes in precipitation. For example, changes in the seasonal cycle of precipitation, even *without changes in the annual mean precipitation*, often lead to changes in $\delta^{18}O_p$ because in many places there is a large seasonal cycle in the $\delta^{18}O$ of precipitation; similarly changes in the pathways and/or the condensation/evaporation cycling of water vapor enroute to a site where the precipitation occurs will also change $\delta^{18}O_p$ without necessarily changing the seasonal cycle of precipitation. Hence, interpretation of the $\delta^{18}O_c$ data from the speleothems requires the use of a climate model that explicitly simulates the time history of the water isotopes $H_2{}^{16}O$ and $H_2{}^{18}O$.

In this study, we employ an atmospheric general circulation model (AGCM) with an embedded scheme for water isotopes and couple it to a 50m slab ocean to examine the impact of the insolation forcing on the tropical climate. We perform two core simulations that represent the extremes in the insolation over the past 950,000 years. We first document the simulated differences in the $\delta^{18}O_p$ and climate, and compare them to the differences in the $\delta^{18}O_c$ from the speleothems (section 3). We then analyze the model isotope data to discern the reasons for the changes in the $\delta^{18}O_c$, and examine the dynamics associated with the simulated climate changes (section 4). We will show that the model captures the gross pattern and amplitude of the orbital signal seen in the caves across Asia. These isotopic changes reflect a fundamental change in the balance of processes that combine to set the maximum near-surface equivalent potential temperature θ_e (which determines the location of monsoon precipitation) during times of high summertime insolation compared to low insolation (such as in today's climate). In section 5.1 we compare and discuss our model precipitation and isotopic results to those previously published. In sections 5.2, 5.3 and 5.4, we further discuss the observed speleothem records and compare our model results with other proxy data that inform on the climate changes associated with insolation forcing. Section 6 contains a summary.

2. The Data, the Climate Model and the Core Experiments

2.1. The Data

The speleothem data are taken from the NOAA National Climate Data Center (NCDC) for Paleoclimatology (www.ncdc.noaa.gov/paleo/paleo.html). The original references for the data are indicated in Table 1. The NCDC data contribution numbers are as follows: Soreq and Peqiin #2003-061; Hulu #2004-023; Sanbao #2009-127; Kesang #2012-006; Tianmen #2010-110; and Sofular #2009-132. The Hoti and Mukalla records show punctuated periods of growth, and age uncertainties in these records preclude using these data past 82 kbp and 129 kbp, respectively. Data for Hoti were not available in digital form. The insolation calculations are from *Huybers* [2006].

2.2. The Climate Model

We employ the ECHAM4.6 AGCM [*Roeckner et al.*, 1996] with a module for water isotopes [*Hoffmann and Heinmann*, 1997; *Hoffmann et al.*, 1998; *Werner et al.*, 2001]. The model is run at T42 (about 250km) resolution and is coupled to a slab ocean. The model is first run with modern-day insolation and modern-day boundary conditions: 360ppm CO_2, and modern-day continental geometry, orography and ice sheets. A cyclo-stationary climatological heat flux ("q-flux") is added to the slab ocean to take into account the heat flux convergence due to unresolved ocean dynamics and errors in the model's surface energy balance. All of the experiments are run for at least 40 years, with output from the last 30 years used to construct climatologies and climatological differences. All differences discussed in this paper are statistically significant at $p = 0.05$ or better.

The model, when forced by modern-day insolation (the Modern-Day experiment), produces seasonal cycles in temperature, precipitation and circulation that agree well with observations. We compare the precipitation simulated by the coupled model with modern-day boundary conditions with that observed (for northeastern Africa and Tibet, see also Figure 9). Figure 2 shows the JJA climatological precipitation from (a) the ECHAM4.6 model forced by modern-day geometry and insolation and (b) from observations. Figure 3 is the same as Figure 2, but for DJF. Overall, the model does quite well at simulating the modern-day seasonal cycle of precipitation – particularly over tropical South America, all of Africa and over land and ocean in the northern half of the Indian Ocean sector. Model biases include too much (little) precipitation in the Atlantic Intertropical Convergence Zone (ITCZ) in JJA (DJF), too much precipitation in the southern Indian Ocean, and too much precipitation just north of the equator in the western Pacific.

2.3. The Core Experiments

Two core experiments are performed that represent the extremes in the northern hemisphere summertime insolation over the past 950,000 years; i.e., they represent NH summers at perihelion and aphelion when eccentricity is large (within $< 0.1\%$, the obliquity parameter is unchanged in the two core experiments). We will refer to these experiments with the interchangeable labels *"high-insolation", "high phase", or "218 kbp"* for the first experiment, and *"low-insolation", "low phase" or "207 kbp"* for the second experiment. In the high-insolation experiment, we force the model with insolation from 218 kbp, which features an extreme maximum NH JJA insolation. In the low-insolation experiment, we forced the model with insolation from 207 kbp, the time of extreme minimum in NH JJA insolation (see, e.g., Figure 1). In both experiments we used modern-day boundary conditions. The difference in the insolation incident at the top of the atmosphere is shown in Figure 4: differences in the NH summer are in excess of $+70$ W/m^2. Additional experiments were also performed, and will be discussed when appropriate.

It is useful to point out that in the NH, the JJA difference maps "high- minus low-insolation" (i.e., "218 minus 207 kbp insolation") shown in Figures 5, 8, and 12 can also be roughly interpreted as the difference between times of high insolation compared to the modern climate. This is because in the NH the JJA insolation at 207 kbp is similar to today (see Figure 4). Hence, it is not surprising that the NH summertime climate simulated by the model forced by low-insolation (207 kbp experiment) is very similar to that from the modern experiment. This is illustrated by the difference map for JJA precipitation in the low-insolation and Modern-Day experiments, shown in Figure A1(a).

3. Results from the Core Experiments

Figure 5 shows the difference in JJA surface temperature and precipitation due to the difference in insolation, "218 kbp minus 207 kbp". As expected, temperatures in the midlatitude continental regions of the NH are up to 9°C greater in the high insolation experiment. There are remarkable and fundamental changes in the location of wet regions in the tropics that signal a shift in the balance of processes that contribute to the near-surface equivalent potential temperature (discussed in Section 4.2) that underpins the location of monsoonal precipitation. Precipitation increases by more than 5 mm/day in a band extending from central sub-Sahara Africa, to across the Arabian Peninsula and into northern India; decreases of more than 5 mm/day extend across southeast Asia and over the Bay of Bengal (see also Figure 8(a)). In effect, the heavy monsoon precipitation has shifted from over southeast Asia in the low-insolation experiment (and from where it is today; see Figures 2 and A2) to be over the land regions in northern India and northeastern Africa. Precipitation across the tropical northern Atlantic Ocean has decreased from 12 mm/day in the low-insolation/modern experiments, to 6 mm/day in the high-insolation experiment (see also Figure A2). The enhanced precipitation center in northeast Africa is associated with a strengthening of the easterly winds along the equator in the Indian Ocean and into the northwest Indian Ocean (Figure 8(a)), while the northward extension and the enhancement of precipitation over the Sahel causes a switch from weak easterly winds to westerly winds along in the Sahel and a collapse of the equatorial Trade Winds across the Atlantic (Figures 5(b), 8(a) and A2).

Figure 6 shows the difference in DJF temperature and precipitation. Cooling in the subtropical NH is a direct response to low-insolation (see Figure 4). Despite the similar winter insolation in the NH, the Arctic is warmer in the high-insolation experiment because the large sea ice melting in summer (compared to 207 kbp) reduces by half the average wintertime sea ice concentration [*Jackson and Broccoli*, 2003]. Precipitation increases in the subtropical southern hemisphere (SH) in the Indian and Pacific Oceans associated with the warmer oceans which are a result of the delayed ocean response to increased springtime insolation.

The changes in $\delta^{18}O_p$ between high- and low-insolation are shown in Figures 7 and 8(b). The model is able to capture the gross aspects of the changes seen in the proxy paleoclimate records, both in terms of the amplitude and the general large-scale pattern of the response. The $\delta^{18}O_p$ is lighter by more than -4 ‰ over northeast Africa and the Arabian Peninsula, and by more than -7 ‰ over Tibet. Superposed in red numbers on Figure 8(b) is the difference in $\delta^{18}O_c$ associated with high-minus-low insolation, inferred from the scaled $\delta^{18}O_c$ at the cave sites (see discussion in section 1). Over the NH, the pattern of $\delta^{18}O_p$ changes is grossly similar to the pattern in precipitation changes (compare Figures 8(a) and 8(b)), although there are important exceptions that we will discuss in Section 4.1.

There are also large changes in the $\delta^{18}O_p$ throughout the tropics and subtropics of the SH that are also somewhat collocated with differences in SH summertime precipitation: negative (positive) $\delta^{18}O_p$ associated with increased (decreased) DJF precipitation (see Figures 6(b) and 7). This pattern of $\delta^{18}O_p$ changes over tropical South America is corroborated by the $\delta^{18}O_c$ changes from speleothems that are sufficiently long to resolve orbital time scales; these results will be presented in a separate paper [*X. Liu et al.*, 2014].

4. Analysis

In this section, we present analyses to illuminate the causes of the $\delta^{18}O_c$ changes in the speleothems, and of the changes in the patterns of precipitation and monsoon dynamics.

4.1. Isotopes and Precipitation

The two 'centers of action' in the simulated pattern of the $\delta^{18}O_p$ changes over Tibet and northeast Africa are corroborated by the $\delta^{18}O_c$ from the stalagmites (see Figure 8(b)). Figure 9 verifies that the model reproduces the modern observed annual cycle in precipitation (see also section 4.3), and hence we can use its output to explore the causes of the simulated 218 kbp minus 207 kbp (or high- minus low-insolation) changes in $\delta^{18}O_p$ in both these regions. We do this by modifying the calculation of $\delta^{18}O_p$ for the 218 kbp case by selectively including or removing the changes in P and $\delta^{18}O$ from specific seasons. For example, to isolate the impact of changes in $\delta^{18}O_p$ due to just the changes in precipitation during the monsoon months (June to September, or JJAS) precipitation, we calculate:

$$\delta^{18}O_p(218\ \mathrm{JJAS\ precip}) - \delta^{18}\mathrm{O_p}(207) = \frac{\sum_m \delta^{18}O_{m,207} \cdot \widetilde{P}_m}{\sum_m \widetilde{P}_m} - \frac{\sum_m \delta^{18}O_{m,207} \cdot P_{m,207}}{\sum_m P_{m,207}} \tag{3}$$

where $\widetilde{P}_m$ contains the non-monsoon months (Oct - May) precipitation from the low-insolation experiment and the monthly precipitation from the monsoon months of the high-insolation experiment. Results are summarized in Table 2.

Averaged over Tibet (26-32.5°N, 85-95°E) and northeast Africa (12-21°N, 25-45°E), the difference in $\delta^{18}O_p$ due to high-minus-low-insolation is -6.28 ‰ and -3.73 ‰, respectively. For both regions, the differences are mainly due to monsoon-season differences (compare values in the middle column of Table 2). And of the two variables that contribute to the

$\delta^{18}O_p$, it is the differences in the JJAS $\delta^{18}O$ of precipitation that is primarily responsible for the climatological changes in $\delta^{18}O_p$. This is at first rather surprising, as there is nearly a doubling of summertime precipitation over Tibet – and nearly a four-fold increase over northeast Africa – in the high-insolation experiment (Figure 9a,b). The explanation lies in the extreme seasonality of precipitation: there is so little precipitation in winter in these regions that $\delta^{18}O_p$ is predominantly determined by the $\delta^{18}O$ of summertime precipitation and therefore it is insensitive to the changes in the total amount of summer precipitation. Indeed, the unimportance of precipitation for $\delta^{18}O_p$ is illustrated in the last column of Table 2: changes in precipitation amount contribute only +1.18 (-1.15) ‰ to the total $\delta^{18}O_p$ change of -6.28 (-3.73) ‰ in Tibet (northeast Africa). Since the $\delta^{18}O_c$ in speolothems is a measure of $\delta^{18}O_p$, these results suggest that these cave records cannot be used to infer changes in the amount of summer precipitation. We note that, consistent with our results, *Vuille et al.* [2005] showed that the year-to-year variations in the observed $\delta^{18}O_p$ in an ice core taken from southern Tibet (Dasuopu, 28°23' N, 85°43' E, 7200m a.s.l.) are highly correlated with variations in the strength of the Indian Ocean/Southeast Asian monsoon, and mainly reflect changes in the isotopic composition of the precipitation; correlations with the amount of precipitation are of secondary importance. Encouragingly, *Vuille et al.* [2005] also confirmed that the year-to-year variations in $\delta^{18}O_p$ over Tibet in the observed (instrumental) data are reproduced by the same model that we use in our study.

Nonetheless, as the pattern and amplitude of the insolation-forced differences in $\delta^{18}O_c$ in the speleothem records are similar to the simulated differences in $\delta^{18}O_p$, the former *are* clearly indicators of large changes in the Indian and southeast Asian summer monsoon due to insolation forcing. Based on the aforementioned results, however, the speloethems record differences in the summer $\delta^{18}O$ of precipitation, and not in the amount of precipitation. Further analysis of our model results suggests that the changes in the $\delta^{18}O$ in the precipitation over Tibet are exclusively due to changes in the $\delta^{18}O$ of the vapor that is imported and subsequently condensed and deposited to the ground. This conclusion is reached by an analysis of the $\delta^{18}O$ of daily precipitation (Figure 10) and an examination of the change in the $\delta^{18}O$ of the vertically averaged water vapor, shown in Figure 11(a). First, Figure 10(a) shows that in the low-insolation experiment the $\delta^{18}O$ of precipitation in Tibet depends only weakly on the intensity of precipitation, measured by the daily accumulated precipitation; in the high insolation experiment, the $\delta^{18}O$ of precipitation actually increases with increasing intensity. Hence, there is little evidence for the "amount effect" in either the low and high insolation experiments (see *Lee and Fung* [2008] for a thorough discussion of the "amount effect"). By contrast, the $\delta^{18}O$ of the daily summertime precipitation is systematically reduced by 3 to 8 ‰ across all precipitation rates from 1 mm/day to 30 mm/day, accounting for 92% (97%) of the total summertime precipitation in the high (low) insolation experiment. Figure 11(a) shows that in the high insolation experiment the isotopic composition of the water vapor over Tibet is 6 ‰ lighter (in the vertical average, and throughout the vertical column), which accounts for the 7 ‰ difference in $\delta^{18}O$ of the precipitation (Figure 9c) and for the change in $\delta^{18}O_p$ (Figure 11(b)). Hence, the change in $\delta^{18}O_p$ over Tibet is due entirely to changes in efficiency of distillation in the Indian monsoon region, which determines the $\delta^{18}O$ of the vapor that is delivered and is subsequently precipitated over Tibet. Though the total summertime precipitation over Tibet increases greatly from the low to high insolation (by

73‰; figure 9a), the "amount effect" is not acting; the changes in cave $\delta^{18}O_c$ register changes in Indian monsoon intensity and not local changes in the amount or intensity of local precipitation.

Over northeast Africa, Figure 11(a) shows the vapor is depleted by only 1 to 3 ‰ and therefore cannot fully account for the ∼4 ‰ change in $\delta^{18}O_p$ in that region. Indeed, over northeast Africa, Figure 10(b) shows the $\delta^{18}O$ of precipitation is strongly dependent on the intensity of precipitation, in both the high and low insolation experiments, and the probability distribution of daily precipitation amounts shows a shift towards more frequent heavy precipitation events in the high insolation experiment compared to the low insolation experiments (Figure 10d). Hence, the "amount" effect does partially account for the differences in the $\delta^{18}O$ of summer precipitation in northeast Africa.

4.2. Dynamics

As discussed in Section 3, there is a fundamental shift in the location of the monsoon precipitation – from southeast Asia and the Bay of Bengal in the low-insolation experiment, to over the land regions extending from north of the Sahel, into northeast Africa and extending eastward into northern India in the high-insolation experiment (Figure 8(a) and A2). For the low-insolation climate, the monsoon dynamics is very similar to that operating in the modern climate and is predominantly due to seasonal variations in insolation and to atmosphere-ocean interaction. Specifically, the monsoon onset happens when the insolation forcing creates a sufficient meridional gradient in subcloud moist entropy (or nearly equivalent, in near-surface equivalent potential temperature, θ_e) so that the near-equatorial ITCZ and attendant Hadley circulation gives way to a precipitation centroid in northern Indian Ocean and southeast Asia [*Prive and Plumb*, 2007a, b; *Bor-*

doni and Schneider, 2008; *Boos and Kuang*, 2010]. Once off the equator, the location of precipitation is predominantly set by the location of the maximum near-surface θ_e [*Prive and Plumb*, 2007a, b]. In observations (Figure 12(a)) and in our model forced by modern-day and 207 kbp insolation (not shown) these maxima are in the Bay of Bengal and throughout southeast Asia. For an overview of the modern thermodynamical view of the monsoon system, see *Molnar et al.* [2010] and references therein.

The same physics operates in the high phase of the insolation cycle. An important difference, however, is that in the high phase the rate of change of the insolation forcing is much greater than in the low phase (see e.g., Figure 4). As such, the early summer near-surface temperature increases over land much faster than over ocean due to the greatly different thermal inertia of land and ocean. Hence, the land-ocean temperature difference is amplified – so much so that the maximum in near-surface θ_e immediately preceding the onset of the summer monsoon is shifts from over the ocean to over the land. Specifically, it is shifted from the ocean regions in the Bay of Bengal and the NW Indian Ocean in the low-insolation and Modern-Day experiments (and in the observations), to be over the land regions of northern India and northeast Africa in the high-insolation experiment where it remains throughout the monsoon season (cf, Figures 12(b) and 12(c)).

4.3. Additional Experiments

Although the basic physics responsible for the land-centric monsoon precipitation in the high-insolation case are similar to those acting to set the ocean-centric monsoon precipitation in the low-insolation case and in the modern climate, there is at least one notable difference. In the modern climate, convective heating over the northern Bay of Bengal gives rise to a westward propagating Rossby disturbance that causes cold air advection aloft and to the west of the convection that is balanced by subsidence, which helps to suppress summer precipitation [*Rodwell and Hoskins*, 1996] and renders the eastern Mediterranean a desert where the atmosphere looses net energy to space in summer; this same physics is operating in the low-insolation experiment (see Figure 13).

We performed an additional experiment with ECHAM4.6 AGCM whereby the model was forced by the low-insolation and an external, localized convective heat source added over northern India to mimic the heating in the high-insolation experiment: otherwise, the experiment was identical to the low-insolation experiment. The results showed that precipitation was reduced by about half over southeast Asia (consistent with that in the 218 kbp experiment, Figure 8(b)), but the subsidence over the eastern Mediterranean was a very small fraction of that observed; Liu and Hoskins obtained a similar results using a different AGCM (B.J. Hoskins, pers. comm., 2011). Thus, although the insolation forcing in the high-insolation experiment appears to be sufficient to cause the maximum in θ_e to be over land, the displacement of the precipitation center from the Bay of Bengal to be over northern India greatly attenuates the desertification mechanism of *Rodwell and Hoskins* [1996]. The movement of heavy precipitation from ocean to land and the accompanying high cloud cover turn northeast Africa and the Arabian Peninsula from a net sink of energy in the low-insolation and Modern-Day experiments, to a net source of energy in the high-insolation experiment (see Figure 13); a similar result was found by *Braconnot et al.* [2008] in their 126 kbp experiment (which features an increase of 62.2 Wm^{-2} in net absorbed summer insolation compared to present day).

The only major difference between the simulated $\delta^{18}O_p$ and observed $\delta^{18}O_c$ that is difficult to reconcile is in east central China, where the simulated orbital signal is ~ 1 ‰

but the observed change is ~ 3.8 ‰. We ruled out model resolution as an explanation for the weak model response, by repeating the two core experiments (207 kbp and 218 kbp) at higher resolution (T106, ~ 120 km). All of the insolation forced changes in climate and isotopic composition discussed in our paper are reproduced using the high-resolution experiments. We revisit the discrepancy between simulated and observed $\delta^{18}O_p$ in eastern China in Section 5.4.

The dominant local insolation signal in the tropical records we have focused on suggest $\delta^{18}O_p$ in these regions is relatively insensitive to the presence of the ice sheets or to glacial – interglacial swings in the concentration of atmospheric carbon dioxide. To evaluate this in the model, we re-ran the core experiments with high- (218 kbp) and low- (207 kbp) insolation, only replacing the modern-day boundary conditions with (i) the LGM continental geometry and orography, including the ice sheets (ICE5G reconstruction, [*Peltier*, 2004]), (ii) 200 ppm CO_2, and (iii) with both LGM orography and 200 ppm CO_2. In all three cases, the response to insolation forcing extremes in the tropics and subtropics was virtually identical to results presented in this paper, which used modern-day geometry and 360 ppm CO_2. These results will be presented elsewhere [*Roe et al.*, 2014], as they are useful for interpreting the climatological significance of isotopic records from the tropics and extratropics during the Pleistocene.

5. Discussion

5.1. Comparison with other model results

5.1.1. Precipitation

The pattern of changes in $\delta^{18}O_p$ and precipitation in our experiments differs from those seen in the pioneering experiments of the impact of the insolation forcing on the monsoons by *Prell and Kutzbach* [1987], *Prell and Kutzbach* [1992] and *Jouzel et al.* [2000], particularly throughout southeastern and eastern Asia and over the Indian Ocean. *Prell and Kutzbach* [1987] and *Prell and Kutzbach* [1992] used early variants of the NCAR Community Climate Model to examine the difference in climate for two periods of high minus low summer insolation: mid-Holocene (6 kbp) minus modern, and 126 kbp minus 115 kbp. They find that compared to today, times of high insolation feature centers of increased precipitation (+2mm/day) over SE Asia and Sahel, whereas our model features centers of increased precipitation ($>$ 5 mm/day) in NE Africa and northern India, and a center of decreased precipitation ($<$ -5 mm/day) over SE Asia. *Jouzel et al.* [2000] examined the changes in annual $\delta^{18}O_p$ associated with the mid-Holocene (6 kbp) and modern climate simulated by the NASA/GISS AGCM and in the same version of the ECHAM AGCM that we used in this study. Unlike our results, the GISS model simulated an incoherent pattern of $\delta^{18}O_p$ change associated with the mid-Holocene to present insolation change, with no change in the vicinity of the Indian Ocean basin, while ECHAM model simulated depletion in the mid-Holocene over central Africa and along the equator in the Indian Ocean (over Tibet and eastern China, the change in $\delta^{18}O_p$ in the ECHAM model is similar to our results). Although the choices for times of high and low insolation that are contrasted in those studies differ from the ones we examine, the most likely explanation for the discrepancies in the results presented in these early studies and our results is that the earlier studies used uncoupled AGCMs forced by prescribed, modern-day sea surface temperatures, so precipitation is strongly constrained and precludes the coupled atmosphere-ocean thermodynamics that is now understood to underlie the modern-day Indian monsoon (see discussion and references in section 4.2). In addition, the AGCMs used in the pioneering studies by *Prell and Kutzbach* [1987] and *Prell and Kutzbach* [1992] have low horizontal resolution that does not adequately isolate the Indian Ocean from the continental regions to the north (see *Boos and Kuang* [2010] for how the Himalaya act as a wall that helps to intensify the Indian monsoon by keeping dry continental air out of the Indian Ocean basin).

There have been two model intercomparison projects whereby the impact of changes in insolation between the present day and mid-Holocene (6 kbp) have been examined: Paleoclimate Modeling Intercomparison Project phase 1 and 2 (PMIP-1 and PMIP-2). The experimental setup in PMIP-1 also used fixed modern-day sea surface temperature (SST) for the mid-Holocene experiments [*Joussaume et al.*, 1999]. Nonetheless, most models showed an increase in precipitation over northern India and, not surprising, an increase in precipitation in the Sahel [*Braconnot et al.*, 2002; *Zhao and Harrison*, 2012] although the increase in northern Africa was not sufficient to explain the reconstructed vegetation [*Kohfeld and Harrison*, 2000]. Grossly similar results are obtained over the Sahel by *Prell and Kutzbach* [1987] in their fixed SST AGCM experiments force by high and low insolation (126 and 115 kbp insolation, respectively), although due to the low resolution used in their experiments, a comparison between their results and those from PIMP-1 or our results is not meaningful.

The second phase of the Paleoclimate Modeling Intercomparison Project (PMIP-2) performed the same mid-Holocene experiment as in PMIP-1, but used a different set of AGCMs and included coupling to ocean models. In general, the pattern of precipitation changes in the mid-Holocene compared to modern-day (high-minus-low insolation phases) found in the PMIP-2 experiments is similar to that from our high and low insolation experiments. A notable difference between the PMIP-2 and PMIP-1 simulations is an amplification in the increase in the precipitation across the Sahel and in northeast Africa in the mid-Holocene that is attributed to interactions between the atmosphere and ocean [*Braconnot et al.*, 2007; *Zhao and Harrison*, 2012] (see also *Liu et al.* [2003] and *Hewitt and Mitchell* [1998]). From the figures in *Braconnot et al.* [2007] and *Zhao and Harrison* [2012], it appears that the amplitude of the precipitation changes over the Sahel, northeast Africa and in the Indian Ocean in the PMIP-2 experiments is roughly one-quarter of that seen in our high- minus low-insolation experiments – which implies a roughly linear response to the amplitude in the insolation forcing (the difference in 30°N JJA insolation 218 kbp minus 207 kbp is 72.5 $\mathrm{Wm^{-2}}$, while the difference between 6 kyr and today is 22.2 $\mathrm{Wm^{-2}}$). Analysis of experiments we performed using insolation every 1 kyr between 195 kbp and 218 kbp also suggest a nearly linear response in monsoon precipitation to changes in JJA insolation (see section 5.4).

Liu et al. [2003] performed time slice experiments for various times during the Holocene using FOAM, a low resolution coupled climate model, while *Braconnot et al.* [2008] performed simulations for various times during the Holocene and the Eemian (the last interglacial period) using the ISPL_CM4 coupled atmosphere-ocean model. In both of these models, precipitation over equatorial Africa and India scales roughly linearly with summer NH insolation, with an amplitude that compares favorably to what is found in our model. The pattern of summer precipitation changes in these two models is somewhat similar to that from our model: precipitation increases (decreases) in northern India (southeast Asia) when summer insolation is increased. However, in both the FOAM and ISPL_CM4 models, the changes in precipitation over Africa are confined to the Sahel and equatorial east Africa; they do not extend farther northward or into the central Arabian Peninsula (c.f. Figure 3 in *Braconnot et al.* [2008] and Figure 5c in *Liu et al.* [2003] with our Figure 5). For a further discussion of how coupling affects the response of the monsoon to insolation forcing in FOAM and the ISPL_CM4 model, see *Liu et al.* [2003] and *Marzin and Braconnot* [2009a, b].

Finally, we note that *Merlis et al.* [2013] performed experiments to evaluate the impact of insolation forcing on the Hadley circulation and zonally averaged precipitation using a simplified atmosphere model coupled to a slab ocean with a prescribed q-flux and with a zonally uniform continent in the subtropics of one hemisphere (say, the NH). Their results are at odds with our model results, *vis-a-vis* changes in the zonally averaged precipitation and the strength of the Hadley circulation – both in the seasonal and annual average. Two likely reasons for the differences are (i) cloud radiative feedbacks which are included in the ECHAM model, and (ii) east-west asymmetries in land the distribution in the NH; both are fundamental to the changes in the monsoon circulation in our experiments, but are excluded in the idealized model/ experiments.

5.1.2. Isotopic composition of precipitation

Schmidt et al. [2007] perform simulations of the modern-day and the mid-Holocene climate with the GISS Model E-R coupled climate model and show patterns of summer precipitation and $\delta^{18}O_p$ change that are roughly similar to those found in our model, although precipitation changes in their simulations are greatest in western equatorial Africa and the anomalies in $\delta^{18}O_p$ extend throughout the bulk of northern Africa whereas our model shows changes mainly in northeastern Africa[2]. Similarly, *LeGrande and Schmidt* [2009] perform time-slice experiments spanning the Holocene with same coupled model

(GISS Model E-R) and show that the increase in $\delta^{18}O_c$ in speleothems in India and China throughout the Holocene is consistent with the simulated increases in $\delta^{18}O_p$. Their results compare favorably to ours: a $\sim 1‰$ in $\delta^{18}O_p$ associated with a 27 Wm^{-2} decrease in summer insolation over the Holocene; over India, the $\delta^{18}O_p$ reflects the intensity of local monsoon precipitation; and poleward of the Indian Ocean, the $\delta^{18}O_p$ mainly reflects the $\delta^{18}O$ of precipitation and is not correlated with local precipitation amount.

Liu et al. [2014] performed time-slice experiments (snapshots) every 1kyr from 21 kbp to present using a low-resolution (T31) version of the isotope-enabled NCAR Community Atmosphere Model, version 3 (CAM3). Each snapshot was forced by 50 years of SST and sea ice taken from a continuous integration of the fully coupled CCSM, forced by the history of atmospheric CO_2, orbital changes in insolation, prescribed ice sheet evolution, and prescribed fresh water fluxes into the ocean. In eastern China, the simulated $\delta^{18}O_p$ closely follows summer insolation and the effect of changing ice volume on ocean $\delta^{18}O$. In eastern China, their central result is similar to ours: local precipitation is maximum during high insolation (the early Holocene) and a minimum during low insolation (21 kbp and late Holocene), and although the local $\delta^{18}O_p$ is out of phase with precipitation in southeastern China, they too find that $\delta^{18}O_p$ in eastern China predominately registers changes in the strength of the Indian Ocean monsoon.

Finally, *Herold and Lohmann* [2009] used the same AGCM model as we do and compared the climate and isotopic composition of precipitation over Africa and central Asia during a time of high summer insolation (124 kbp, during the Eemian) with a time of relatively low insolation (the modern climate). This represents a difference in summer insolation of ~ 44.4 Wm^{-2} – twice that of the difference between mid-Holocene and today, and about two-thirds the difference between 218 kbp and 207 kbp. Although their experiments are uncoupled, they prescribe SST boundary conditions that are taken from the output of a coupled model (though without an isotope module) forced by the 124 kbp and modern-day insolation forcing, respectively. Encouragingly, the pattern of the changes in $\delta^{18}O_p$ and summer precipitation they report are very similar to those we have found, and the amplitude of the response scales roughly linearly with the change in summer insolation (compare their Figures 3a and 9b with our Figure 7). Consistent with our findings, they also find that precipitation in northeast Africa increases when summer insolation is high mainly due to eastward advection of vapor originating from the tropical Atlantic (see their Figures 2a and 3a).

5.2. Comparison of our model results with the speleothem data

In this section, we compare the changes in $\delta^{18}O_p$ simulated by our model to the amplitude of $\delta^{18}O_c$ changes recorded in the long spelothems listed in Table 1 and shown in Figure 8(b); a discussion of the results for the Hulu/Sanbao site is deferred to section 5.4.

The amplitude of the orbital signal in $\delta^{18}O_p$ simulated by our model is in good agreement with the speleothem $\delta^{18}O_c$ records from Israel (Peqiin/Soreq), Oman (Hoti), Yemen (Mukulla), Turkey (Solufar), and from Tibet (Tianmen). *Bar-Matthews* [2003] and *Bar-Matthews et al.* [1997, 2000] present the Peqiin and Soreq cave records, respectively, and note that the negative excursions of $\delta^{18}O_p$ are coincident with the high summertime insolation, and indicate enhanced annual mean precipitation. Our model simulates a 84% increase in the annual average precipitation at 218 kbp compared with 207 kbp, while *Bar-Matthews* [2003] estimate a maximum insolation increase of 70% above modern precipitation during marine isotope stage 5, based on the observed relationship between

$\delta^{18}O_p$ and precipitation, and inferred changes in vegetation from the $\delta^{13}C$ excursions in the speleothems.

Burns et al. [1998] found stalagmites in Hoti Cave in Oman that grew in the early Holocene and during the last interglacial. They argued that the lighter $\delta^{18}O_c$ in these stalagmites (compared to modern-day $\delta^{18}O_p$) indicates increased wetness in the Arabian Peninsula during interglacial conditions. We note, however, that both periods of stalagmite growth are also coincident with periods of high summertime insolation. That they did not find stalagmites that formed during the last glacial period could be due to a threshold effect (hypothesized drying during the ice age created too dry conditions for stalagmite formation, even during times of high summertime insolation), or perhaps it is an example of the adage "absence of evidence is not evidence of absence." Indeed, *Burns et al.* [2001] and *Fleitmann* [2003] later found stalagmites in Hoti Cave that dated to 80 kbp – also coincident with the high phase of the summer insolation cycle – as well as speleothems that grew during the penultimate glacial period. The difference between the $\delta^{18}O_c$ in the Hoti Cave stalagmites that grew in times of high insolation and the $\delta^{18}O_c$ in modern-day stalagmites is $\sim$ 3 - 4 ‰, which compares favorably to $\delta^{18}O_p$ change simulated by the model ($\sim$ 4 ‰). Finally, *Fleitmann* [2003] conclude that the source of the water during these wet periods must be distal to the cave site, based on the stalagmite deuterium, and suggest a tropical Indian Ocean source. Although our model also indicates a distal source for the moisture, the predominant source of moisture in eastern Africa and Arabian Peninsula in our high-insolation simulation is the tropical Atlantic via northeast Africa, which is in agreement with the source of moisture in the 6 kbp simulation of *Patricola and Cook* [2007]. *Fleitmann et al.* [2011] reported the history of stalagmite growth in Mukalla

Cave in Southern Yemen is similar to that seen in Hoti Cave farther north in Oman: speleothems grew during the current and last interstadial, as well at 80 kbp (in Makalla Cave, dating uncertainties are too large to determine the phasing of earlier stalagmite growth relative to the orbital cycles).

Consistent with the interpretation of *Pausata et al.* [2011] and *Cai et al.* [2010], we find that the insolation driven in $\delta^{18}O_p$ measured on the Tibetan plateau are solely due to changes in the summer monsoon intensity over the Indian Ocean sector, which affects the isotopic composition of the vapor imported to Tibet. There is a large change in the net summer precipitation over Tibet, but this cannot be directly inferred from the cave isotopes (see discussion in section 4.1). Although the amplitude of the insolation induced $\delta^{18}O_p$ changes at Tianmen in Tibet in the model agree well with those observed ($\sim$7 ‰), we note that the speleothems in Tianmen stop growing during the low summer insolation, perhaps due to lack of water. Hence, the amplitude of the orbital signal in $\delta^{18}O_c$ in Tianmen may be a lower limit on the actual swings in $\delta^{18}O_p$ (see *Cai et al.* [2010] for further discussion).

As mentioned in section 1, the $\delta^{18}O_c$ in speleothems from Sofular Cave in Turkey is not correlated with insolation over the duration of the record, 50 kyr; this is in agreement with our model results (see Figure 8(b)). *Fleitmann et al.* [2009] show that the Sufular record clearly tracks $\delta^{18}O$ in the Greenland ice core (including the abrupt millennial scale changes). We can't rule out, however, that a longer record from Turkey would show an orbital signature: over the last 50 kyr, the Sofular and Hulu/Sanbao records are very similar and yet when the whole of the Hulu/Dongee record examined, there is a clear orbital signal in the latter record (see Figure 1 and Table 1).

Finally, the observed changes in $\delta^{18}O_c$ at Kesang in northwestern China are comparable to those at Tianmen. The large response in $\delta^{18}O_p$ simulated by our model are confined to the high Tibetan Plateau, whereas the Kesang site is far to the north – poleward of the Tarim Basin. Although *Cheng et al.* [2012] ascribe the large Kesang signals to be a measure of the strength of the incursion of the Asian summer monsoon into this region, it could be that it could be that the Kesang site is recording changes in the wintertime storm track that influences this region. In that case, the failure of our model to capture the orbital signal at Kesang could be due to an erroneously southward displacement of the wintertime storm track simulated by the model in the high-insolation experiment, or due to model errors in the fractionation efficiency under very low temperatures (below -20°C) due to the joint presence of ice crystals and supercooled water.

5.3. Comparison with other proxy data and their interpretations

In this section, we compare our model results to all other proxy data that we are aware of for which the records are sufficiently long and the chronology sufficiently constrained so that the orbital signal (or lack thereof) can be assessed.

Rossignol-Strick [1983] and *Rossignol-Strick* [1985] suggest the sapropel formations in the eastern Mediterranean Sea are due to unusually high inputs of freshwater into the eastern Mediterranean associated with enhanced summer precipitation over the Ethiopian highlands during the high phase of the summer insolation cycle that is subsequently brought to the sea via the Nile River. This is remarkably consistent with our model results (see Figure 8(a)). *Bar-Matthews et al.* [2000] and *Bar-Matthews* [2003] note that eight of the nine sapropel formations observed in the past 240 kyr are coincident with times of wet conditions in the Israeli caves and all occur during high summertime insolation.

Kroon et al. [1998] argue that sapropel formation in the eastern Mediterranean has been orbitally paced for at least the past 3.2 million years.

In addition to the sapropel data and the orbital pacing of the times of speleothem growth discussed in section 5.2, a myriad of proxy indicators consistently show wetter conditions in the Middle East in the early Holocene (a time of high summer insolation) compared to the late Holocene (a time of low summer insolation); these include proxy records of vegetation [*Jolly et al.*, 1998a], lake levels [*Jolly et al.*, 1998b] and of Red Sea salinity [*Arz et al.*, 2003]. There is some discussion in the literature of whether the wetter mean conditions in times of high summer insolation reflect changes in summer, winter or annual mean precipitation; see *Kutzbach et al.* [2014] for a comprehensive discussion. In our model, there is nearly a two-fold increase in annual precipitation in the far eastern Mediterranean and in the Middle East, and almost all of this increase is in summertime (as in the simulations of *Kutzbach et al.* [2014], the ECHAM model shows an increase in winter precipitation but it is much smaller than the increase in summer precipitation). The increase in summer precipitation is sufficiently large that the maximum precipitation shifts from wintertime in the low insolation experiment (and in today's climate), to summertime in the high insolation experiment. Further support for a summertime precipitation change is found in the agreement between the amplitude of the orbital $\delta^{18}O_c$ signal in the Middle Eastern caves and the insolation-forced changes in $\delta^{18}O_p$ simulated by the model. In the model, $\delta^{18}O_p$ in the Middle East is depleted in the high insolation case due to the "amount effect" (see Figure 11(b)): summertime precipitation is isotopically lighter than in winter because the precipitation is associated with more intense precipitation than in winter.

Schulz et al. [1998] presented one sediment core record from the northwest Arabian Sea that was sufficiently long ($\sim$ 110 kyr) that the insolation signal could clearly be identified in the $\delta^{18}O_c$ in the shells of the formaminifer *Globigerinoides ruber* (although an insolation signal is not obvious in two shorter records ($\sim$ 60 kyr) farther to the east, which appear to be more similar to the Greenland ice cores). They interpret this record as an indictor of sea surface temperature regulated by the the strength of the upwelling (southwesterly) monsoon winds in the Arabian Sea – stronger winds associated with the greater summertime insolation, which is consistent with our results (see Figure 8(a)).

Reichart et al. [1998] and *Clemens et al.* [2010] report that total organic carbon production in the northern Arabian Sea is also orbitally paced, with maximum production lagging the maximum summertime insolation by $\sim$3 kyr and $\sim$5 kyr respectively[3]. *Bassinot et al.* [2011] forced an offline biogeochemical-ecophysiological model with the output from simulations performed by *Marzin and Braconnot* [2009a] of the 9kr (high summer insolation) and 6 kbp climate using the ISPL_CM4 coupled atmosphere-ocean model. They reproduced the observed phasing of primary production in the western and eastern Arabian sea relative to the insolation forcing throughout the Holocene and showed that the changes in both regions are consistent with the changes in the monsoonal winds. *Reichart et al.* [1998] note that the total organic carbon production in the northern Arabian Sea today is sensitive to the *duration* of the upwelling favorable winds in the monsoon (rather than the strength of the winds). Our results indicate the onset time of the monsoon is relatively insensitive to the phase of the insolation (not shown). Since the orbital modulation of the end-of-summer insolation lags that of the mid-summer insolation by $\sim$3 kyr, this would explain the high correlation between summer-averaged insolation and the 3 kyr lagged productivity records.

Molfino and McIntyre [1990] examine a 200 kyr sediment core (RC24-7) from the equatorial Atlantic (1°20.5'S, 11°53.3'W). They report a strong orbital signal, with greater SST and lower productivity associated with June perihelion (high JJA insolation); in turn, this implies reduced upwelling along the equator in the Atlantic in JJA (the high productivity season). Our modelling results are consistent with this. Figures 5(b) and A2 show that the equatorial Atlantic Trade Winds collapse in JJA due to the enhanced monsoonal circulation over central equatorial Africa.

Finally, we note that the pattern and amplitude of the $\delta^{18}O_p$ response to insolation forcing over South America agrees remarkably well with the $\delta^{18}O_c$ in speleothems in the Andes (Huagapo Cave, *Kanner* [2012]), northeast Brazil (Rio Grande du Norde Cave, *Cruz et al.* [2009]) and southeast Brazil (Botuvera Cave, *Wang et al.* [2004, 2007]). Orbitally paced differences in $\delta^{18}O_c$ are reported to be +3 ‰ (Andes), -4 ‰ (northeast Brazil) and +2 ‰ (southeast Brazil) – very similar to that simulated by our model (see Figure 7). The dynamics responsible for these isotope variations and their climatological significance are discussed in *Liu et al.* [2014].

5.4. What's with the central China speleothems?

Perhaps the only major discrepancy between the speleothem data and the model results is in the lowlands of east central China, where the observed amplitude of the insolation-driven response in $\delta^{18}O_c$ in the speleothems in Hulu/Sanbao (Figure 1) is ~ 4 ‰ while the model simulates only 1 ‰. In addition, the central China $\delta^{18}O_c$ records are unique in suggesting that the response to insolation forcing in this region may not be smooth:

the transitions between the extremes are sometimes abrupt (e.g., at 120, 128, 189, 192, 200 kbp). Taken at face value, this suggests some missing physics in the model.

First, we note that the disagreement between observed $\delta^{18}O_c$ and simulated $\delta^{18}O_p$ is not resolved by enhancing the horizontal resolution of the simulations (see section 4.3). We also performed 22 additional experiments, running the model with observed insolation every 1 kyr, from 195 kbp to 218 kbp (each model run was for 40 years, and we analyzed the last 30 years of integration). The climate and isotope changes associated with the insolation forcing vary smoothly and nearly linearly with insolation – everywhere on the planet. Indeed, the first empirical orthogonal function of $\delta^{18}O_p$ (the first eigenvector of the $\delta^{18}O_p$ covariance matrix) from all 24 experiments captures 78% of the total variance in $\delta^{18}O_p$ and reproduces the pattern of isotope change as is seen in Figure 7; the first principle component is almost identical in shape to JJA insolation at 30°N). We note that *Kutzbach et al.* [2008] also found that the changes in climate vary smoothly with insolation forcing in a 280 kyr continuous integration of a low-resolution coupled climate model. Hence, a possible explanation for the model-observation discrepancy in central China is that insolation forcing produces smooth swings in $\delta^{18}O_p$ in eastern China with a peak-to-peak amplitude of ~ 1 ‰ (consistent with our model results), but the lions' share of the 4 ‰ total orbital signal is accomplished by abrupt threshold physics that is not captured by our model. Below we offer two suggestions, but reject one of them outright.

One possibility is that insolation forcing causes slow changes in the mean state of the global ocean in such a way that the ocean undergoes a stability threshold, causing sea ice extent to change greatly and abruptly in the North Atlantic, thereby changing the climate and $\delta^{18}O_p$ abruptly throughout the northern hemisphere (see *Pausata et al.* [2011]). We reject this idea, however, because the only known phenomena that are purportedly associated with abrupt sea ice extent are the Dansgaard-Oscheger oscillations and Heinrich events that are clearly evident in proxy records in Israel and in the Arabian Sea – locations where the proxy data show a clear insolation signal and yet no such abrupt changes coincident with the insolation-paced abrupt changes seen in the speleothems in central China.

Absent any plausible idea or evidence for a global abrupt change, a more likely scenario is that the abrupt insolation-coordinated changes in China are due to local processes that are missing in our model. One suggestion is that insolation forcing causes smooth changes in climate in eastern China: our model suggests a $\sim$50% increase in precipitation and 2°C increase in temperature in summer in the high-insolation experiment compared to the low-insolation experiment. In turn, the smooth changes in climate cause threshold changes in vegetation and/or soil properties that affect evaporation and/or the flow of water through the soil that cause abrupt changes in the fractionation of soil water as it percolates to the cave. For example, one might envision the warmer, wetter climate at high summer insolation would support forest vegetation, whereas a colder, drier climate would support grasslands. Similarly, a smooth change in the amount of precipitation may cause an abrupt change in the flow rate through the soils and thus evaporation (even without vegetation changes) which could affect the fractionation of water as it makes the journey from the surface to the cave. In these scenarios, the lion's share of the insolation signal in cave $\delta^{18}O_c$ is recording abrupt changes in evaporation via abrupt changes in vegetation/soil water holding capacity while a lesser and smoother contribution is due directly to the climate changes (i.e., to the changes in the $\delta^{18}O$ of precipitation). Some support for this hypothesis is found in relationship between the $\delta^{18}O_c$ and $\delta^{13}C$ in the stalagmites in Hulu cave: $\delta^{18}O_c$ and $\delta^{13}C$ are negatively correlated and abrupt changes in $\delta^{18}O_c$ and coincident with abrupt changes in $\delta^{13}C$ [*Kong et al.*, 2005]. We note, however, that the *Kong et al.* [2005] record does not extend back far enough in time to determine whether the abrupt transitions in $\delta^{18}O_c$ evident in Figure 1 are also seen in $\delta^{13}C$.

6. Summary

We have performed modelling experiments with the ECHAM4.6 AGCM coupled to a slab ocean to examine the impact of insolation forcing on the climate and the isotopic composition of precipitation. The amplitude and pattern of the insolation-forced changes in the precipitation-weighted $\delta^{18}O$ of precipitation ($\delta^{18}O_p$) compares favorably to the pan-Asian signature in the oxygen isotopic composition of the calcite ($\delta^{18}O_c$) in speleothems spanning from Israel eastward to the Saudi Arabian Peninsula and Tibet. Compared to times of low summer insolation in the NH, high insolation forcing features $\delta^{18}O_p$ over northeast Africa/Saudi Arabia and Tibet that is depleted by 4 ‰ and 7 ‰, respectively. In these regions, the model results suggest that stalagmites are records of the changes in the isotopic composition of the summertime precipitation. Summertime precipitation over Tibet is depleted in times of high northern hemisphere summer insolation because of the vapor that is arriving is depleted due to changes in the intensity of the Indian Monsoon (see also *Pausata et al.* [2011]). Over northeastern Africa, monsoon precipitation is depleted because the vapor that is arriving from the west is depleted and because of changes in the probability distribution of the intensity of precipitation (the so-called amount effect). A robust conclusion of our analyses is that the strong seasonal cycle in precipitation in these regions renders $\delta^{18}O_p$, and hence $\delta^{18}O_c$, quite insensitive to changes in the total amount of summer precipitation (Table 2).

Theory and observations indicate that the large-scale monsoonal precipitation will be located over the maximum in near-surface θ_e [*Prive and Plumb*, 2007a, b; *Bordoni and Schneider*, 2008; *Boos and Kuang*, 2010]. Our model results suggest that in the northern hemisphere, times of low summer insolation (near June aphelion) – such as in the modern climate – feature an Indian and southeast Asian monsoon that are largely a result of the heating of southeast Asia and the atmospheric response to increasing θ_e over the ocean in the northern Indian Ocean; the heating of the land is not sufficiently competitive to shift the maximum θ_e from ocean to land.

In times of high summer insolation in the northern hemisphere (i.e, June perihelion), the monsoon circulation is fundamentally different. Insolation increases sufficiently quickly from late winter to early summer that the land - ocean temperature difference becomes very large and the location of the maximum θ_e shifts toward land along the northwest and northern Indian Ocean basin. Hence the maximum in summer precipitation shifts from southeast Asia and the Bay of Bengal (where it is in today's climate; see Figure 2) to land regions extending from northeast Africa eastward to Pakistan and over northern India. This shift is aided by a reduction in the subsidence over the Middle East that is driven when the precipitation center is over the Bay of Bengal [*Rodwell and Hoskins*, 1996]. Times of high summer insolation feature a greater summer maximum in near-surface θ_e and therefore a more intense Indian monsoon, which accounts for the depleted vapor that is advected northward to Tibet and thus the depleted $\delta^{18}O_c$ at Tianmen.

There is a notable discrepancy between our model results and the speleothem records in eastern central China (Hulu and Sanbao caves), where observations show a 4 ‰ depletion in $\delta^{18}O_c$ during the high summer insolation and the model shows only a 1 ‰ depletion. In this region, the speleothems are unique among the world's cave records in that most of the 4 ‰ change in $\delta^{18}O_c$ between orbitally-paced extremes is often accomplished abruptly; if these abrupt changes are excised from the records, then the model results and observations are in agreement. Thus, we raise the possibility that the $\delta^{18}O_c$ records in east-central China represent the smooth modest (~ 1 ‰) change in $\delta^{18}O_p$ and in climate that we see in our model, and these climate changes give rise to an abrupt change in vegetation that are signaled by an abrupt 3 ‰ change in $\delta^{18}O_p$ that is subsequently recorded in the stalagmite $\delta^{18}O_c$.

We note that our model also reproduces the amplitude and pattern of the insolation-driven cycles in $\delta^{18}O_c$ in the speleothems across tropical South America. The climatological interpretation of these records and the dynamics responsible for the changes in climate and isotopic composition of precipitation across tropical South America are presented in [*X. Liu et al.*, 2014].

Appendix A: Approximating $\delta^{18}O$ by $\delta^{18}O_p$

The climatological $\delta^{18}O$ of a sample is (see equation 1):

$$\delta^{18}O \equiv \left\{ {C_s}^{-1} \frac{^{18}O}{^{16}O} - 1 \right\} \times 1000, \tag{A1}$$

where ^{18}O and ^{16}O are the moles of the oxygen isotope in a sample (in our case, precipitation), and C_s is the ratio of ^{18}O to ^{16}O in the standard (in our case, $C_s = 2.0052 \times 10^{-3}$ for Standard Mean Ocean Water). To better understand the relative contributions of changes in precipitation and changes in the $\delta^{18}O$ of precipitation to the changes in the $\delta^{18}O$ recorded in the speleothems, in the paper we approximate equation A1 as

$$\delta^{18}O \cong \frac{\sum_m \delta^{18}O_m \cdot P_m}{\sum_m P_m} \equiv \delta^{18}O_p, \tag{A2}$$

where $\delta^{18}O_m$ is the $\delta^{18}O$ for the month m (i.e., Equation A1 applied to month m) and P_m is the total precipitation for month m.

Let $^{18}O_m$ be the moles of ^{18}O that are delivered in the precipitation in month m; similarly $^{16}O_m$ be the moles of ^{16}O. The mass of precipitation for the month (in grams) is then

$$P_m = 20 \times {}^{18}O_m + 18 \times {}^{16}O_m. \tag{A3}$$

Now we can rewrite equation A1 as follows:

$$C_s \left\{ \delta^{18}O \times 10^{-3} + 1 \right\} \equiv \frac{^{18}O}{^{16}O} = \frac{\sum_m {}^{18}O_m}{\sum_m {}^{16}O_m}. \tag{A4}$$

We note that $^{18}O_m/^{16}O_m$ is of $\mathcal{O}(C_s)$.

Now consider our approximate equation A2, which we can rewrite using equations A1 and A3 as

$$\delta^{18}O_p = \frac{\sum_m ({C_s}^{-1} \frac{^{18}O_m}{^{16}O_m} - 1) \times 1000 \times P_m}{\sum_m P_m}, \tag{A5}$$

or

$$C_s \left\{ \delta^{18}O_p \times 10^{-3} + 1 \right\} = \frac{\sum_m \frac{^{18}O_m}{^{16}O_m} P_m}{\sum_m P_m}. \tag{A6}$$

Substituting equation A3 into the right hand side of equation A6 we obtain

$$\frac{\sum_m \frac{^{18}O_m}{^{16}O_m} P_m}{\sum_m P_m} = \frac{\sum_m {}^{18}O_m \left(1 + \mathcal{O}\left(\frac{^{18}O_m}{^{16}O_m}\right)\right)}{\sum_m {}^{16}O_m \left(1 + \mathcal{O}\left(\frac{^{18}O_m}{^{16}O_m}\right)\right)} = \frac{^{18}O}{^{16}O} \left(1 + \mathcal{O}(\frac{^{18}O_m}{^{16}O_m})\right), \tag{A7}$$

and so equation A6 becomes

$$C_s \left\{ \delta^{18}O_p \times 10^{-3} + 1 \right\} = \frac{^{18}O}{^{16}O} (1 + \mathcal{O}\left(C_s\right)). \tag{A8}$$

Comparing equation A8 to equation A4, we see that the error in approximating the climatological $\delta^{18}O$ (equation A1) with the precipitation weighted $\delta^{18}O$ (equation A2) is of order of $\mathcal{O}\left(C_s\right)$, or about 0.2%.

Appendix B: Seasonal Results from the 207 kbp and 218 kbp experiments

Figure A1 shows the difference in the climatological precipitation from the low-insolation (207 kbp) experiment and the modern-day insolation experiment, for the northern hemisphere summer (JJA) and winter (DJF) seasons. Figure A1(a) shows that low-insolation experiment features summertime precipitation that is very similar to that in the modern-day climate: differences in precipitation are typically less than 20% of the modern-day precipitation. In comparison, Figure 5(b) shows there are large differences in precipitation in the high-insolation experiment compared to the low-insolation experiment (and to the Modern-Day experiment; not shown), including fundamental shifts in all of the centers of action for the monsoonal precipitation. These results are expected because the NH insolation at 207 kbp is very similar to the modern-day NH insolation, wheres the 218 kbp insolation differs greatly from modern-day insolation (see Figure 4). Similar results are obtained for temperature: there are minor differences in the JJA temperature in the low-insolation and Modern-Day experiments (not shown), while the differences in JJA temperature between the high- and low-insolation experiments are large (see Figure 5(a)). This is consistent with the small differences in insolation in the low and Modern-Day experiments compared to that in the high- and low-insolation experiments. Hence, for JJA one can think of the differences between the high- and low-insolation climates as being very similar to the difference between high-insolation and the modern-day climate.

Unlike for NH precipitation in JJA, one cannot use the modern-day precipitation as a reference point for envisioning the difference in precipitation in the high- and low-insolation experiments in the SH summer (DJF): compare Figure A1(b) to 6(b). This is because the DJF insolation at 207 kbp is notably different from modern-day insolation (see Figure 4).

Figure A2 shows the climatological JJA precipitation and 850 hPa winds for the 207 kbp experiment, which features maxima in precipitation over southeast Asia, the equatorial central Indian Ocean and the familiar convergence zone features over the Atlantic and Pacific Oceans. For completeness the climatological JJA precipitation and 850 hPa winds from the 218 kbp experiments is also shown.

Acknowledgments. We thank G. Hoffman for providing the code for ECHAM4.6. DSB is grateful for stimulating discussions with Drs. Xianfeng Wang, Peter Molnar, Gavin Schmidt, John Kutzbach, and Larry Edwards over the course of this work. We also appreciate the official and unofficial reviews of the manuscript by Peter Molnar, Xianfeng Wang, Zhengyu Liu, Vathias Vuille, David McGee and an anonymous reviewer; their thoughtful comments helped us to greatly improve the manuscript. The CERES data were obtained from the NASA Langley Research Center Atmospheric Science Data

Center (https://eosweb.larc.nasa.gov/). This work was supported by the National Science Foundation Division of Earth Sciences Continental Dynamics Programs, award Nos. 0908558 and 1210920. Any model output that has been archived will be made freely available upon request to DSB.

Notes

1. *Frumkin et al.* [1999] show a $\delta^{18}O_c$ record from a cave in Israel that is very similar to the Soreq/Peqiin record, only with more gaps; hence, it is not reproduced here.
2. Unfortunately, it is not possible to compare the relative the amplitude of the changes over Africa and India in the *Schmidt et al.* [2007] simulations because in these regions the anomalies saturate the color bar that is used in their figures.
3. We use JJA insolation, whereas *Clemens et al.* [2010] use June 1 insolation; these insolation curves are offset by ~3 kyr. Using JJA insolation, the phase lag in productivity reported by the *Clemens et al.* [2010] becomes ~ 8 - 3 = 5 kyr.

References

Arz, H., F. Lamy, J. Patzold, P. Muller, and M. Prins (2003), Mediterranean moisture source for an early-Holocene humid period in the northern Red Sea, *Science*, *300*(5616), 118–121, doi:10.1126/science.1080325.

Bar-Matthews, M. (2003), Sea-land oxygen isotopic relationships from planktonic foraminifera and speleothems in the Eastern Mediterranean region and their implication for paleorainfall during interglacial intervals, *Geochimica et Cosmochimica Acta*, *67*(17), 3181–3199, doi:10.1016/S0016-7037(02)01031-1.

Bar-Matthews, M., A. Ayalon, and A. Kaufman (1997), Late quaternary paleoclimate in the eastern Mediterranean region from stable isotope analysis of speleothems at Soreq Cave, Israel, *Quaternary Research*, *47*, 155–168, doi:10.1006/qres.1997.1883.

Bar-Matthews, M., A. Ayalon, and A. Kaufman (2000), Timing and hydrological conditions of Sapropel events in the Eastern Mediterranean, as evident from speleothems, Soreq cave, Israel, *Chemical Geology*, *169*(1-2), 145–156, doi:10.1016/S0009-2541(99)00232-6.

Bassinot, F. C., C. Marzin, P. Braconnot, O. Marti, E. Mathien-Blard, F. Lombard, and L. Bopp (2011), Holocene evolution of summer winds and marine productivity in the tropical Indian Ocean in response to insolation forcing: data-model comparison, *Climate of the Past*, *7*(3), 815–829, doi:10.5194/cp-7-815-2011.

Boos, W. R., and Z. Kuang (2010), Mechanisms of Poleward Propagating, Intraseasonal Convective Anomalies in Cloud System-Resolving Models, *Journal of Atmospheric Sciences*, *67*(11), 3673–3691, doi:10.1175/2010JAS3515.1.

Bordoni, S., and T. Schneider (2008), Monsoons as eddy-mediated regime transitions of the tropical overturning circulation, *Nature Geoscience*, *1*(8), 515–519, doi:10.1038/ngeo248.

Braconnot, P., B. L. Otto-Bliesner, S. P. Harrison, S. Joussaume, J.-Y. Peterchmitt, a. Abe-Ouchi, M. Crucifix, E. Driesschaert, T. Fichefet, C. D. Hewitt, M. Kageyama, A. Kitoh, a. Laîné, M.-F. Loutre, O. Marti, U. Merkel, G. Ramstein, P. J. Valdes, S. L. Weber, Y. Yu, and Y. Zhao (2007), Results of PMIP2 coupled simulations of the Mid-Holocene and Last Glacial Maximum Part 1: experiments and large-scale features, *Climate of the Past*, *3*(2), 261–277, doi:10.5194/cp-3-261-2007.

Braconnot, P., C. Marzin, L. Gregoire, E. Mosquet, and O. Marti (2008), Monsoon response to changes in Earth's orbital parameters : comparisons between simulations of the Eemian and of the Holocene, *Climate Of The Past*, *4*, 281–294.

Braconnot, P., M. Loutre, B. Dong, S. Joussaume, P. Valdes, and and PMIP Participating Groups (2002), How the simulated change in monsoon at 6 ka BP is related to the simulation of the modern climate: results from the Paleoclimate Modeling Intercomparison Project, *Climate Dynamcis*, *19*(2), 107–121, doi:10.1007/s00382-001-0217-5.

Burns, S. J., A. Matter, N. Frank, and A. Mangini (1998), Speleothem-based paleoclimate record from northern Oman, *Geology*, *26*(6), 499, doi:10.1130/0091-7613(1998)026¡0499.

Burns, S. J., D. Fleitmann, A. Matter, U. Neff, and A. Mangini (2001), Speleothem evidence from Oman for continental pluvial events during interglacial periods, *Geology*, *29*(7), 623, doi:10.1130/0091-7613(2001)029¡0623.

Cai, Y., H. Cheng, Z. An, R. L. Edwards, X. Wang, L. Tan, and J. Wang (2010), Large variations of oxygen isotopes in precipitation over south-central Tibet during Marine Isotope Stage 5, *Geology*, *38*(3), 243–246, doi:10.1130/G30306.1.

Cheng, H., R. L. Edwards, W. S. Broecker, G. H. Denton, X. Kong, Y. Wang, R. Zhang, and X. Wang (2009), Ice age terminations, *Science (New York, N.Y.)*, *326*(5950), 248–52, doi:10.1126/science.1177840.

Cheng, H., P. Z. Zhang, C. Spötl, R. L. Edwards, Y. J. Cai, D. Z. Zhang, W. C. Sang, M. Tan, and Z. S. An (2012), The climatic cyclicity in semiarid-arid central Asia over the past 500,000 years, *Geophysical Research Letters*, *39*(1), 1–5, doi:10.1029/2011GL050202.

Clemens, S. C., W. L. Prell, and Y. Sun (2010), Orbital-scale timing and mechanisms driving Late Pleistocene Indo-Asian summer monsoons: Reinterpreting cave speleothem delta O-18, *Paleoceanography*, *25*, doi:10.1029/2010PA001926.

Cruz, F. W., M. Vuille, S. J. Burns, X. Wang, H. Cheng, M. Werner, R. Lawrence Edwards, I. Karmann, A. S. Auler, and H. Nguyen (2009), Orbitally driven eastwest antiphasing of SouthAmerican precipitation, *Nature Geoscience*, *2*(3), 210–214, doi:10.1038/ngeo444.

Dayem, K. E., P. Molnar, D. S. Battisti, and G. H. Roe (2010), Lessons learned from oxygen isotopes in modern precipitation applied to interpretation of speleothem records of paleoclimate from eastern Asia, *Earth and Planetary Science Letters*, *295*, 219–230.

Fleitmann, D. (2003), Changing moisture sources over the last 330,000 years in Northern Oman from fluid-inclusion evidence in speleothems, *Quaternary Research*, *60*(2), 223–232, doi:10.1016/S0033-5894(03)00086-3.

Fleitmann, D., H. Cheng, S. Badertscher, R. L. Edwards, M. Mudelsee, O. M. Göktürk, a. Fankhauser, R. Pickering, C. C. Raible, A. Matter, J. Kramers, and O. Tüysüz (2009), Timing and climatic impact of Greenland interstadials recorded in stalagmites from northern Turkey, *Geophysical Research Letters*, *36*(19), 1–5, doi:10.1029/2009GL040050.

Fleitmann, D., S. J. Burns, M. Pekala, A. Mangini, A. Al-Subbary, M. Al-Aowah, J. Kramers, and A. Matter (2011), Holocene and Pleistocene pluvial periods in Yemen, southern Arabia, *Quaternary Science Reviews*, *30*(7-8), 783–787, doi:10.1016/j.quascirev.2011.01.004.

Frumkin, A., D. C. Ford, and H. P. Schwarcz (1999), Continental Oxygen Isotopic Record of the Last 170,000 Years in Jerusalem, *Quaternary Research*, *51*(3), 317–327, doi:10.1006/qres.1998.2031.

Herold, M., and G. Lohmann (2009), Eemian tropical and subtropical African moisture transport: an isotope modelling study, *Climate Dynamics*, *33*(7-8), 1075–1088, doi:10.1007/s00382-008-0515-2.

Hewitt, C., and J. Mitchell (1998), A fully coupled GCM simulation of the climate of the mid-Holocene, *Geophysical Research Letters*, *25*(3), 361–364, doi:10.1029/97GL03721.

Hoffmann, G., and M. Heinmann (1997), Water Isotope Modeling in the Asian Monsoon Region, *Quaternary International*, *37*(96), 115–128.

Hoffmann, G., M. Werner, and M. Heimann (1998), Water isotope module of the ECHAM atmospheric general circulation model: A study on timescales from days to several years, *Journal of Geophysical Research*, *103*(D14), 16,871–16.

Huybers, P. (2006), Early Pleistocene glacial cycles and the integrated summer insolation forcing, *Science*, *313*, 508–511, doi:10.1126/science.1125249.

Jackson, C., and A. Broccoli (2003), Orbital forcing of Arctic climate: mechanisms of climate response and implications for continental glaciation, *Climate Dynamics*, *21*(7-8), 539–557, doi:10.1007/s00382-003-0351-3.

Jolly, D., I. Prentice, R. Bonnefille, A. Ballouche, M. Bengo, P. Brenac, G. Buchet, D. Burney, J. Cazet, R. Cheddadi, T. Edorh, H. Elenga, S. Elmoutaki, J. Guiot, F. Laarif, H. Lamb, A. Lezine, J. Maley, M. Mbenza, O. Peyron, M. Reille, I. Reynaud-Farrera, G. Riollet, J. Ritchie, E. Roche, L. Scott, I. Ssemmanda, H. Straka, M. Umer, E. Van Campo, S. Vilimumbalo, A. Vincens, and M. Waller (1998a), Biome reconstruction from pollen and plant macrofossil data for Africa and the Arabian peninsula at 0 and 6000 years, *Journal of Biogeography*, *25*(6), 1007–1027, doi:10.1046/j.1365-2699.1998.00238.x.

Jolly, D., S. Harrison, B. Damnati, and R. Bonnefille (1998b), Simulated climate and biomes of Africa during the late quaternary: Comparison with pollen and lake status data, *Quaternary Science Reviews*, *17*(6-7), 629–657, doi:10.1016/S0277-3791(98)00015-8.

Joussaume, S., K. Taylor, P. Braconnot, J. Mitchell, J. Kutzbach, S. Harrison, I. Prentice, A. Broccoli, A. Abe-Ouchi, P. Bartlein, C. Bonfils, B. Dong, J. Guiot, K. Herterich, C. Hewitt, D. Jolly, J. Kim, A. Kislov, A. Kitoh, M. Loutre, V. Masson, B. McAvaney, N. McFarlane, N. de Noblet, W. Peltier, J. Peterschmitt, D. Pollard, D. Rind, J. Royer, M. Schlesinger, J. Syktus, S. Thompson, P. Valdes, G. Vettoretti, R. Webb, and U. Wyputta (1999), Monsoon changes for 6000 years ago: Results of 18 simulations from the Paleoclimate Modeling Intercomparison Project (PMIP), *Geophysical Research Letters*, *26*(7), 859–862, doi:10.1029/1999GL900126.

Jouzel, J., G. Ho, R. D. Koster, and V. Masson (2000), Water isotopes in precipitation: data / model comparison for present-day and past climates, *Quaternary Science Reviews*, *19*(1572).

Kanner, L. C. (2012), An isotopic perspective on climatic change in tropical South America from the modern through the Last Glacial period, Ph.D. thesis, University of Massachusetts, 201 pp.

Kohfeld, K., and S. P. Harrison (2000), How well can we simulate past climates? Evaluating the models using global palaeoenvironmental datasets, *Quaternary Science Reviews*, *19*(1-5), 321–346, doi:10.1016/S0277-3791(99)00068-2.

Kong, X., Y. Wang, J. Wu, H. Cheng, R. Edwards, and X. Wang (2005), Complicated responses of stalagmite delta C-13 to climate change during the last glaciation from Hulu Cave, Nanjing, China, *Science in China Series D-Earth Sciences*, *48*(12), 2174–2181, doi:10.1360/04yd0140.

Kroon, D., I. Alexander, M. Little, L. J. Lourens, A. Matthewson, A. H. F. Robertson, and T. Sakamoto (1998), Oxygen isotope and sapropel stratigraphy in the eastern

Mediterranean during the last 3.2 million years, *Arctic*, *160*(1938), 181–189.

Kutzbach, J. E., X. Liu, Z. Liu, and G. Chen (2008), Simulation of the evolutionary response of global summer monsoons to orbital forcing over the past 280,000 years, *Climate Dynamics*, *30*(6), 567–579, doi:10.1007/s00382-007-0308-z.

Kutzbach, J. E., G. Chen, H. Cheng, R. L. Edwards, and Z. Liu (2014), Potential role of winter rainfall in explaining increased moisture in the Mediterranean and Middle East during periods of maximum orbitally-forced insolation seasonality, *Climate Dynamics*, *42*(3-4), 1079–1095, doi:10.1007/s00382-013-1692-1.

Lee, J.-E., and I. Fung (2008), "amount effect" of water isotopes and quantitative analysis of post-condensation processes, *Hydrological Processes*, *22*(1), 1–8, doi:10.1002/hyp.6637.

LeGrande, A. N., and G. A. Schmidt (2009), Sources of holocene variability of oxygen isotopes in paleoclimate archives, *Climate of the Past Discussions*, *5*(2), 1133–1162, doi:10.5194/cpd-5-1133-2009.

Liu, X., D. S. Battisti, and G. H. Roe (2014), The Influence of Precession on the Climate and Isotopic Composition of Precipitation in Tropical South America, *In preparation.*

Liu, Z., B. L. Otto-Bliesner, J. E. Kutzbach, L. Li, and C. Shields (2003), Coupled Climate Simulation of the Evolution of Global Monsoons in the Holocene, *Journal of Climate*, *16*(15), 2472–2490, doi:10.1175/1520-0442.

Liu, Z., X. Wen, E. C. Brady, B. Otto-Bliesner, G. Yu, H. Lu, H. Cheng, Y. Wang, W. Zheng, Y. Ding, R. L. Edwards, J. Cheng, W. Liu, and H. Yang (2014), Chinese cave records and the East Asia Summer Monsoon, *Quaternary Science Reviews*, *83*, 115–128, doi:10.1016/j.quascirev.2013.10.021.

Marzin, C., and P. Braconnot (2009a), The role of the ocean feedback on Asian and African monsoon variations at 6kyr and 9.5kyr BP, *Comptes Rendus Geosciences*, *341* (8-9), 643–655, doi:10.1016/j.crte.2009.09.001.

Marzin, C., and P. Braconnot (2009b), Variations of Indian and African monsoons induced by insolation changes at 6 and 9.5 kyr BP, *Climate Dynamics*, *33* (2-3), 215–231, doi:10.1007/s00382-009-0538-3.

Merlis, T. M., T. Schneider, S. Bordoni, and I. Eisenman (2013), Hadley Circulation Response to Orbital Precession. Part II: Subtropical Continent, *Journal of Climate*, *26* (3), 754–771, doi:10.1175/JCLI-D-12-00149.1.

Molfino, B., and A. McIntyre (1990), Precessional forcing of nutricline dynamics in the equatorial Atlantic, *Science*, *249*, 766–69.

Molnar, P., W. R. Boos, and D. S. Battisti (2010), Orographic Controls on Climate and Paleoclimate of Asia: Thermal and Mechanical Roles for the Tibetan Plateau, in *Annual Review of Earth and Planetary Sciences, Vol 38*, *Annual Review of Earth and Planetary Sciences*, vol. 38, edited by Jeanloz, R and Freeman, KH, pp. 77–102, doi:10.1146/annurev-earth-040809-152456.

Patricola, C. M., and K. H. Cook (2007), Dynamics of the West African monsoon under mid-Holocene precessional forcing: Regional climate model simulations, *Journal of Climate*, *20* (4), 694–716, doi:10.1175/JCLI4013.1.

Pausata, F. S. R., D. S. Battisti, K. H. Nisancioglu, and C. M. Bitz (2011), Chinese stalagmite δ18O controlled by changes in the Indian monsoon during a simulated Heinrich event, *Nature Geoscience*, *4* (7), 474–480, doi:10.1038/ngeo1169.

Peltier, W. (2004), Global glacial isostasy and the surface of the ice-age Earth: The ice-5G (VM2) model and GRACE, *Annual Review of Earth and Planetary Sciences*, *32*, 111–149, doi:10.1146/annurev.earth.32.082503.144359.

Prell, W., and J. Kutzbach (1992), Sensitivity of the Indian monsoon to forcing parameters and implications for its evolution, *Nature*, (360), 647–52.

Prell, W. L., and J. E. Kutzbach (1987), Monsoon Variability Over the Past 150,000 Years, *Journal of Geophysical Research*, *92* (D7), 8411–8425, doi:10.1029/JD092iD07p08411.

Prive, N. C., and R. A. Plumb (2007a), Monsoon dynamics with interactive forcing. Part I: Axisymmetric studies, *Journal of Atmospheric Sciences*, *64* (5), 1417–1430, doi:10.1175/JAS3916.1.

Prive, N. C., and R. A. Plumb (2007b), Monsoon dynamics with interactive forcing. Part II: Impact of eddies and asymmetric geometries, *Journal of Atmospheric Sciences*, *64* (5), 1431–1442, doi:10.1175/JAS3917.1.

Reichart, G., L. Lourens, and W. Zachariasse (1998), Temporal variability in the northern Arabian Sea Oxygen Minimum Zone (OMZ) during the last 225,000 years, *Paleoceanography*, *13* (6), 607–621, doi:10.1029/98PA02203.

Rodwell, M., and B. Hoskins (1996), Monsoons and the dynamics of deserts, *Quarterly Journal of the Royal Meteorological Society*, *122* (534, Part b), 1385–1404, doi:10.1002/qj.49712253408.

Roe, G. H., Q. Ding, and D. S. Battisti (2014), The response of Asian summertime climate to the largest geologic forcing of the past 50 Ma, *In preparation*.

Roeckner, E., K. Arpe, L. Bengtsson, M. Christoph, M. Claussen, L. Dmenil, M. Esch, M. Giorgetta, U. Schlese, and U. Schulzweida (1996), The atmospheric general circulation model ECHAM-4: Model description and simulation of present-day climate, *Max Planck Institut fur Meteorologie Report 218*, (218), 90.

Rossignol-Strick, M. (1983), African monsoons, as immediate climate response to orbital insolation, *Nature*, *304*, 46–48.

Rossignol-Strick, M. (1985), Mediterranean Quaternary sapropels, an immediate response of the African Monsoons to variation of insolation, *Palaeogeogr., Palaeoclim., Palaeoecol*, *49*, 237–253.

Schmidt, G. a., A. N. LeGrande, and G. Hoffmann (2007), Water isotope expressions of intrinsic and forced variability in a coupled ocean-atmosphere model, *Journal of Geophysical Research*, *112*(D10), 1–18, doi:10.1029/2006JD007781.

Schulz, H., U. von Rad, and H. Erlenkeuser (1998), Correlation between Arabian Sea and Greenland climate oscillations of the past 110,000 years, *Nature*, *393*(6680), 54–57.

Schwarcz, H. (2007), Carbonate stable isotopes: Speleothems, in *Encyclopedia of Quaternary Science*, edited by S. A. Elias, pp. 290 – 300, Elsevier, Oxford, doi:10.1016/B0-44-452747-8/00352-5.

Vuille, M., M. Werner, R. S. Bradley, and F. Keimig (2005), Stable isotopes in precipitation in the Asian monsoon region, *Journal of Geophysical Research*, *110*(D23), 1–15, doi:10.1029/2005JD006022.

Wang, X., A. S. Auler, R. L. Edwards, H. Cheng, P. S. Cristalli, P. L. Smart, D. a. Richards, and C.-C. Shen (2004), Wet periods in northeastern Brazil over the past 210 kyr linked to distant climate anomalies., *Nature*, *432*(7018), 740–3, doi: 10.1038/nature03067.

Wang, X., A. S. Auler, R. L. Edwards, H. Cheng, E. Ito, Y. Wang, X. Kong, and M. Solheid (2007), Millennial-scale precipitation changes in southern Brazil over the past 90,000 years, *Geophysical Research Letters*, *34*(23), 1–5, doi:10.1029/2007GL031149.

Wang, Y. J., H. Cheng, R. L. Edwards, Z. S. An, J. Y. Wu, C. C. Shen, and J. a. Dorale (2001), A high-resolution absolute-dated late Pleistocene Monsoon record from Hulu Cave, China, *Science (New York, N.Y.)*, *294*(5550), 2345–8, doi:10.1126/science.1064618.

Werner, M., M. Heimann, and G. Hoffmann (2001), Isotopic composition and origin of polar precipitation in present and glacial climate simulations, *Tellus Series B-Chemical and Physical Meteorology*, *53*(1), 53–71, doi:10.1034/j.1600-0889.2001.01154.x.

Xie, P., and P. Arkin (1997), Global precipitation: A 17-year monthly analysis based on gauge observations, satellite estimates, and numerical model outputs, *Bulletin of the American Meteorological Society*, *78*, 2539–2558.

Zhao, Y., and S. P. Harrison (2012), Mid-Holocene monsoons: a multi-model analysis of the inter-hemispheric differences in the responses to orbital forcing and ocean feedbacks, *Climate Dynamics*, *39*(6), 1457–1487, doi:10.1007/s00382-011-1193-z.

Table 1. Speleothems used in this study and featured in Figures 1 and 8(b). Noted are the cave location, elevation above sea level and the reference for the data; also noted is the oldest data in each record. The amplitude of the insolation signal at Peqiin/Soreq, Hulu/Sanbao and Kesang is found by a linear regression of the measured $\delta^{18}O_c$ against JJA 30°N insolation and then scaled by the difference in JJA insolation, 218 kbp minus 207 kbp, which is 72.5 Wm^{-2}; the 95% confidence interval is noted in parenthesis. Sofular is uncorrelated with insolation and tracks ice volume over the past 50 kyr. For Peqiin/Soreq and Hulu/Sanbao, the (negative) correlation between insolation and $\delta^{18}O_c$ is greater when the ice volume impact on ocean $\delta^{18}O$ is first removed, but not significantly so. The amplitude at Tianmen, Hoti and Mukalla is discussed in section 1.

Cave and Location	Duration	Amplitude	Reference
Peqiin (32°58"N 35°19"E, 650m asl) plus Soreq (31°45"N 35°03E, 400m asl)	184 kyr	-1.6‰ (-1.0, -2.2)	*Bar-Matthews* [2003]; *Bar-Matthews et al.* [1997, 2000]
Hulu (32°30"N 119°10"E; 31°40"N, 100m asl) plus Sanbao (32°40'N 110°27"E, 1900m asl)	224 kyr	-3.8‰ (-3.3, -4.3)	*Wang et al.* [2001]; *Cheng et al.* [2009]
Kesang (42°52"N 81°45"E, 2000m asl)	500 kyr	-3.9‰ (-3.1, -4.7)	*Cheng et al.* [2012]
Tianmen (30°55"N 90°40"E, 4800m asl)	127 kyr	-7‰	*Cai et al.* [2010]
Hoti (23°05"N 57°21"E, 800m asl)	82 kyr	-4‰	*Burns et al.* [1998], *Burns et al.* [2001], *Fleitmann* [2003]
Mukalla (14°55'N 48°35'E, 1500m asl)	129 kyr	-4‰	*Fleitmann et al.* [2011]
Sofular (41°25"N 31°56"E, 700m asl)	50 kyr	0‰	*Fleitmann et al.* [2009]

Table 2. Sources of the difference in precipitation-weighted $\delta^{18}O$ ($\delta^{18}O_p$) averaged over Tibet (26-32.5°N, 85-95°E) and northeast Africa (12-21°N, 25-45°E). The net difference in $\delta^{18}O_p$ due to both the precipitation and $\delta^{18}O$ changes (218 kbp minus 207 kbp) is highlighted in bold. The importance of summer changes is illuminated in the "Summer Only" rows, whereby the $\delta^{18}O_p$ at 218 kbp is calculated using a hybrid time series of precipitation and/or $\delta^{18}O$: summer (June - September) precipitation and/or $\delta^{18}O$ is taken from the 218 kbp simulation, while winter (October - May) precipitation and $\delta^{18}O$ are taken from the 207 kbp simulation. Similarly, the "Winter Only" row illuminates the importance of changes in precipitation and/or $\delta^{18}O$ in the winter months October - May. Column four shows the importance of the change in $\delta^{18}O$ to the change in $\delta^{18}O_p$; it is found by substituting the 207 kbp precipitation into Equation 2 when calculating the 218 kbp $\delta^{18}O_p$. Similarly, column five shows the importance of the change in precipitation to the change in $\delta^{18}O_p$.

Location	Months Used	Δ(precip) and Δ($\delta^{18}O$)	Δ($\delta^{18}O$) only	Δ(precip) only
Tibet	All	**-6.28** ‰	-7.07 ‰	+1.18 ‰
Tibet	Summer Only	-5.45 ‰	-5.21 ‰	+0.86 ‰
Tibet	Winter Only	-0.86 ‰	-1.86 ‰	+0.47 ‰
NE Africa	All	**-3.73** ‰	-3.11 ‰	-1.15 ‰
NE Africa	Summer Only	-3.56 ‰	-2.46 ‰	-1.16 ‰
NE Africa	Winter Only	-0.63 ‰	-0.66 ‰	-0.75 ‰

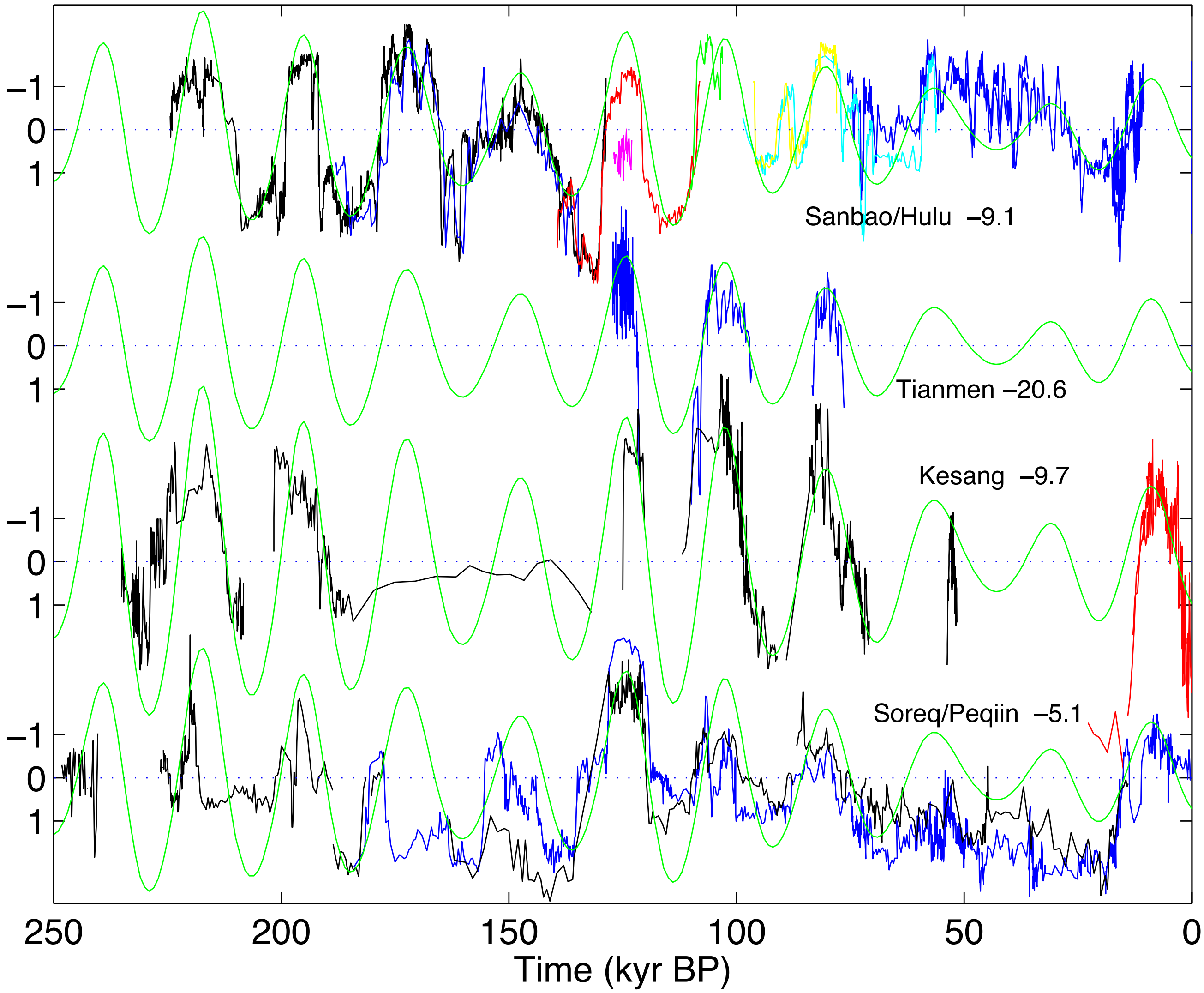

Figure 1. Time series of the oxygen isotopic composition of calcite $\delta^{18}O_c$ (in ‰) in stalagmites across Asia that are sufficiently long to resolve orbital time scales. For each speleothem, the time average $\delta^{18}O_c$ is noted (e.g., Tianmen = -20.6‰) and removed before plotting. Superposed on each speleothem record is the summer (JJA) insolation at 30°N (in green). For ease of viewing, the insolation has been scaled so that the standard deviation of insolation is identical to the standard deviation of the $\delta^{18}O_p$ (in ‰) for the respective cave record. Within a single cave, the records are constructed from several stalagmites, each of which is indicated by a separate color. The cave locations and references for the speleothem data are provided in Table 1.

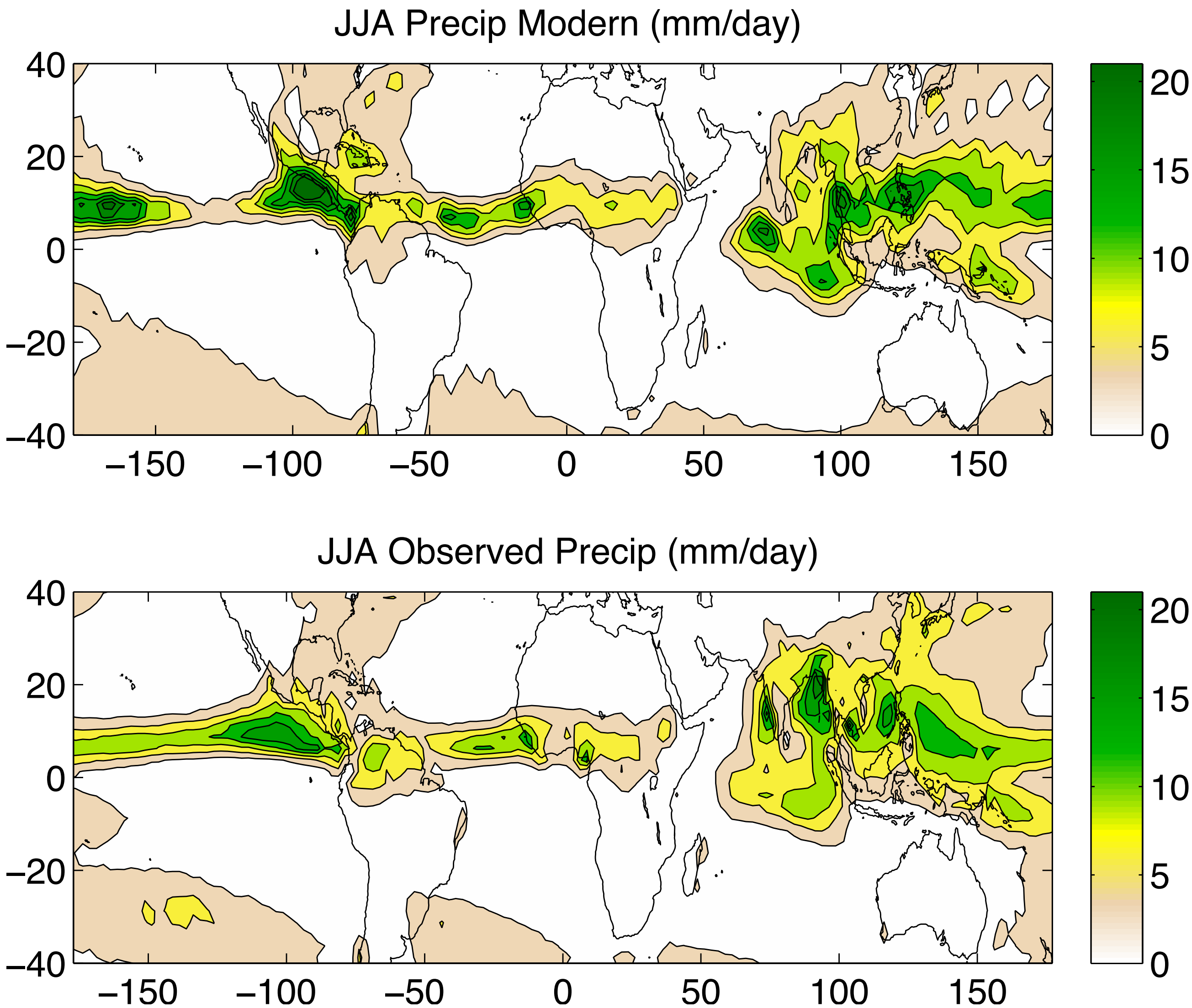

Figure 2. JJA averaged precipiation from the (top) Modern-Day experiment and (bottom) from observations. Observations are taken from the NOAA Climate Prediction Center Merged Analysis of Precipitation (CMAP) product [*Xie and Arkin*, 1997]. Contour inverval is 3 mm/day, starting at 3 mm/day.

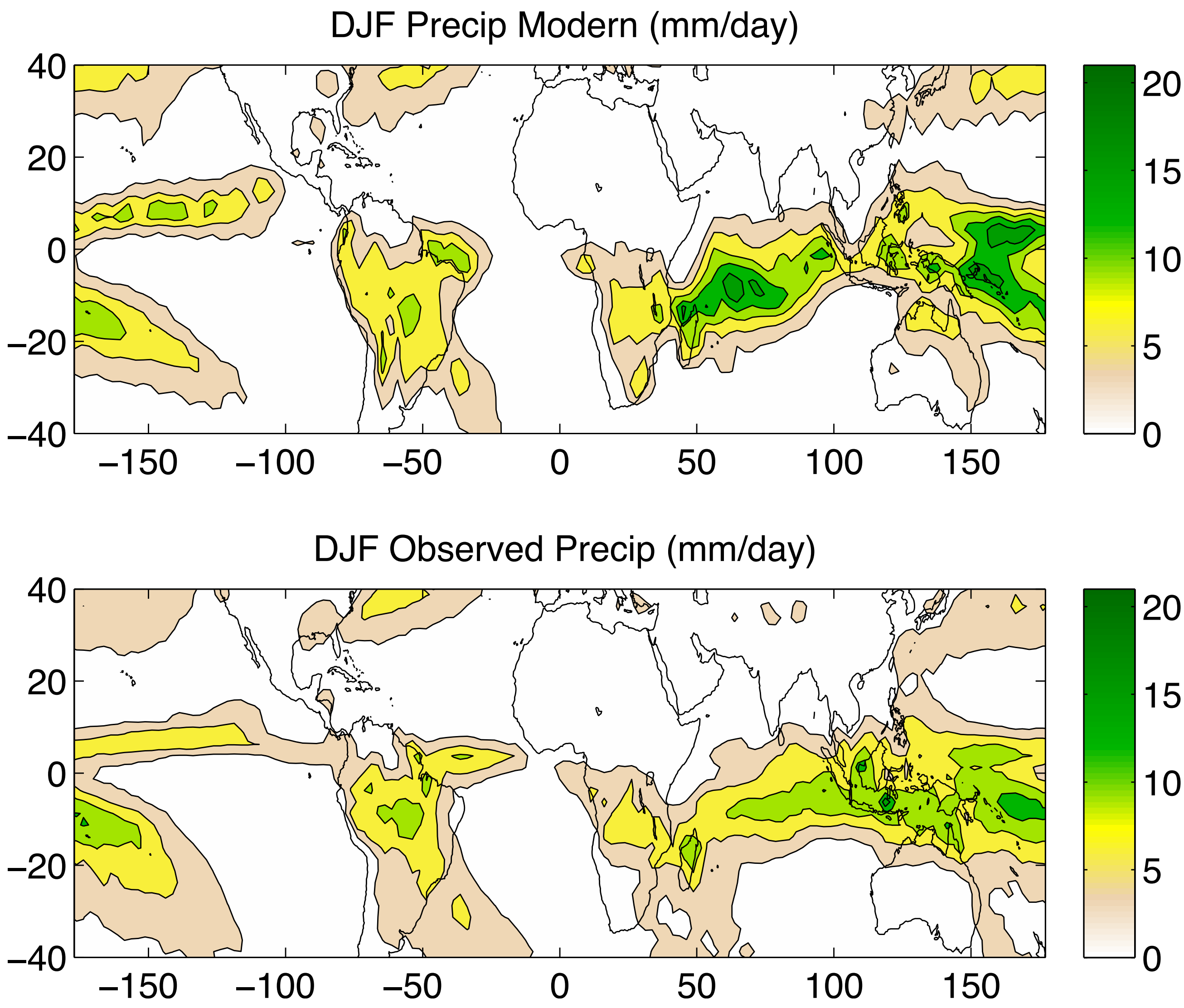

Figure 3. As in Figure 2, but for DJF.

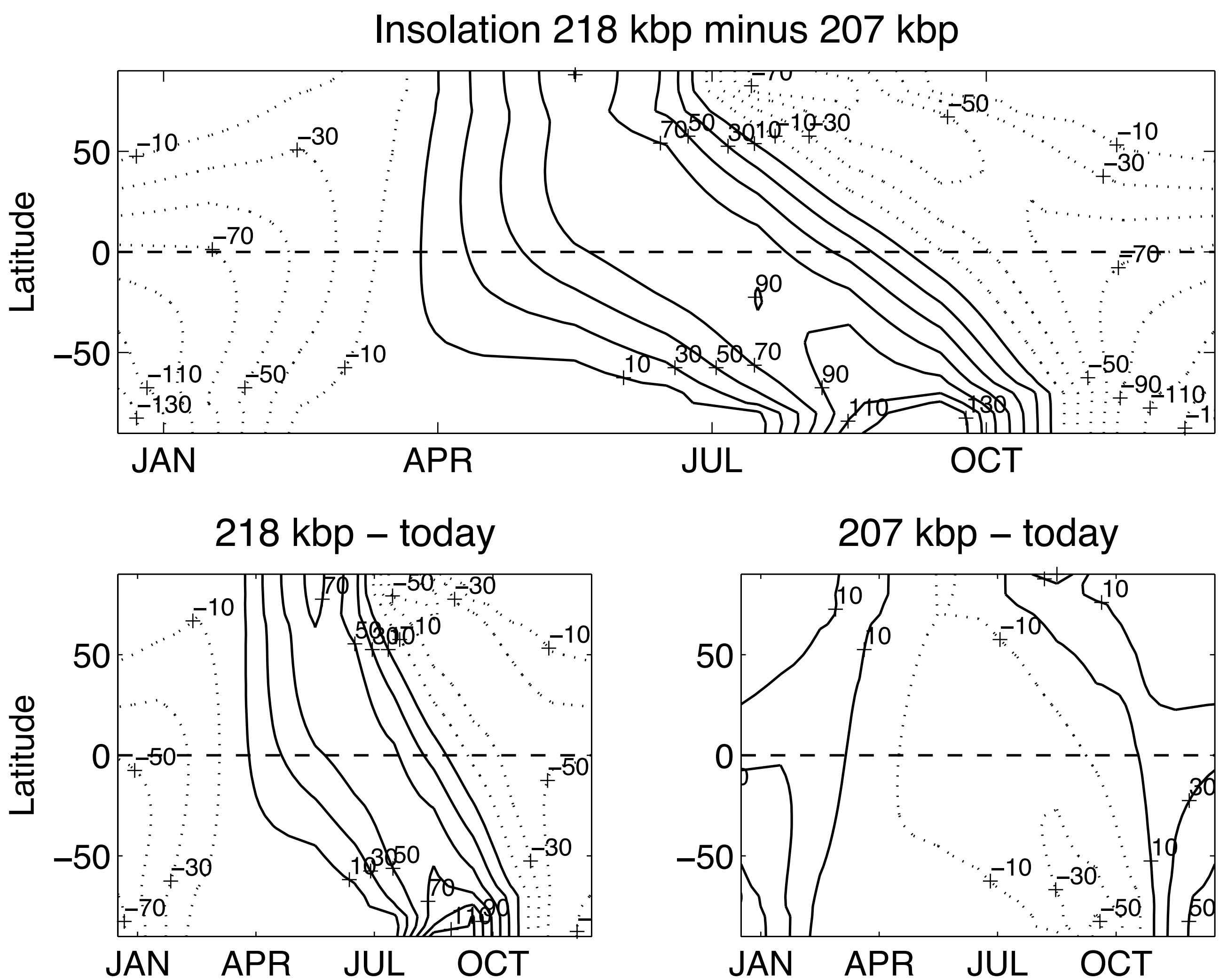

Figure 4. Differences in top-of-atmosphere insolation. Top: 218 kbp minus 207 kbp. Bottom left: 218 kbp minus today. Bottom right: 207 kbp minus today. Note that in the NH the insolation at 207 kbp is similar to that of today.

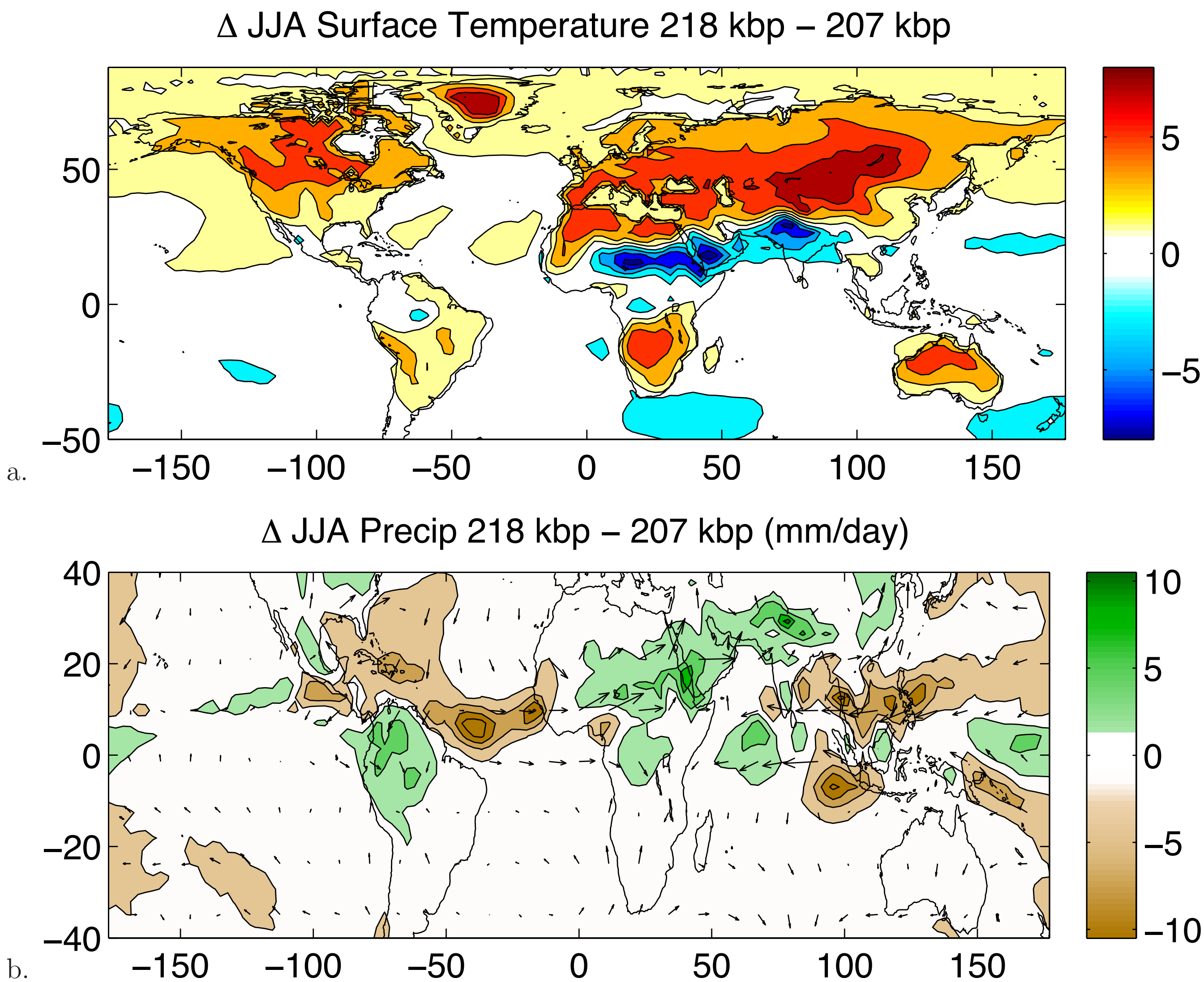

Figure 5. The difference in climate associated with differences in insolation, 218 kbp minus 207 kbp. Summer (JJA) (a) temperature and (b) summer precipitation and 850 hPa wind. The contour interval is 2°C and 3 mm/day for temperature and precipitation, respectively. Differences less than 1°C and 1.5 mm/day are colored white. The maximum wind vector is 8.9 ms^{-1}.

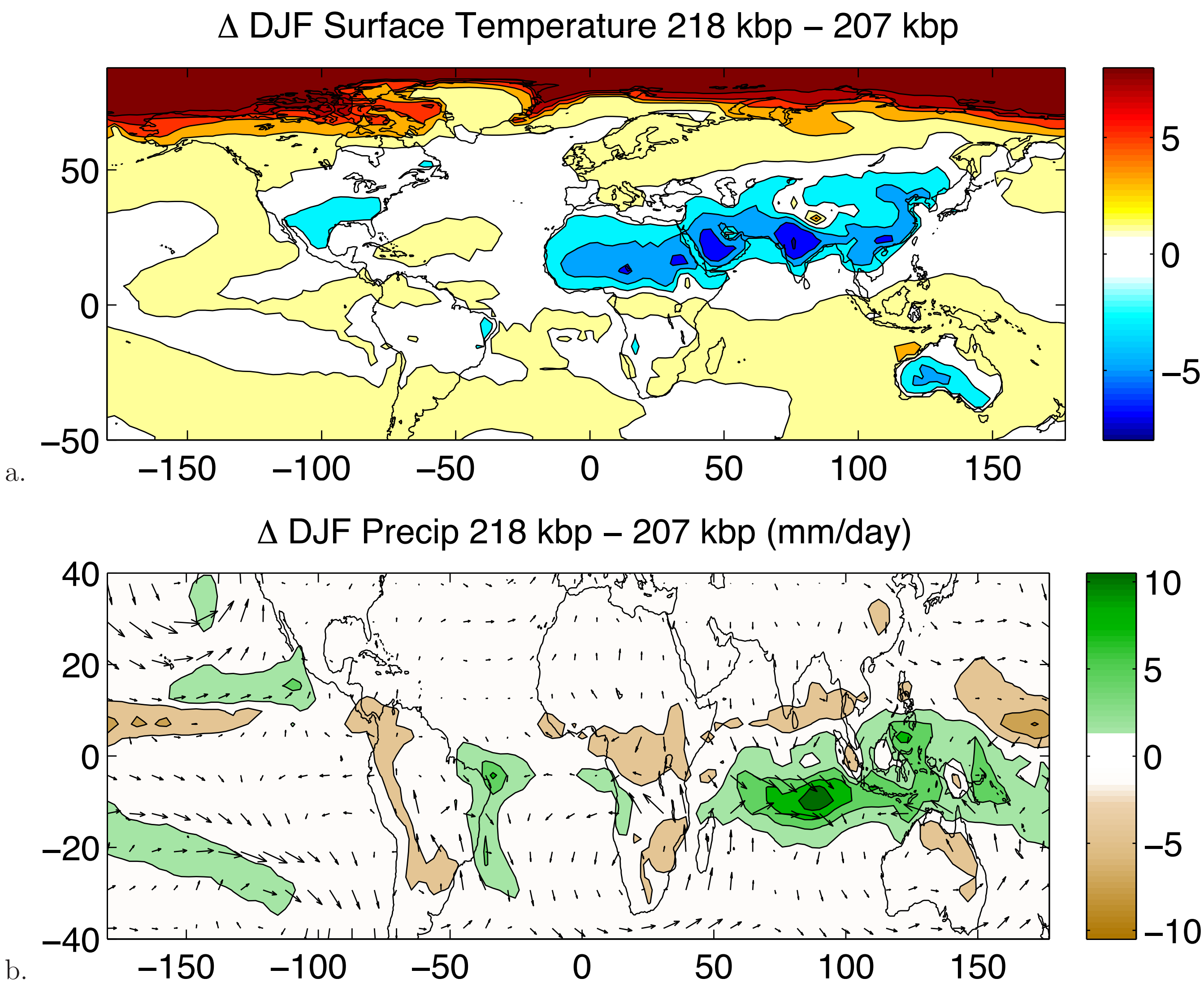

Figure 6. As in Figure 5, but for winter (DJF). The maximum wind vector is 5.9 m/s.

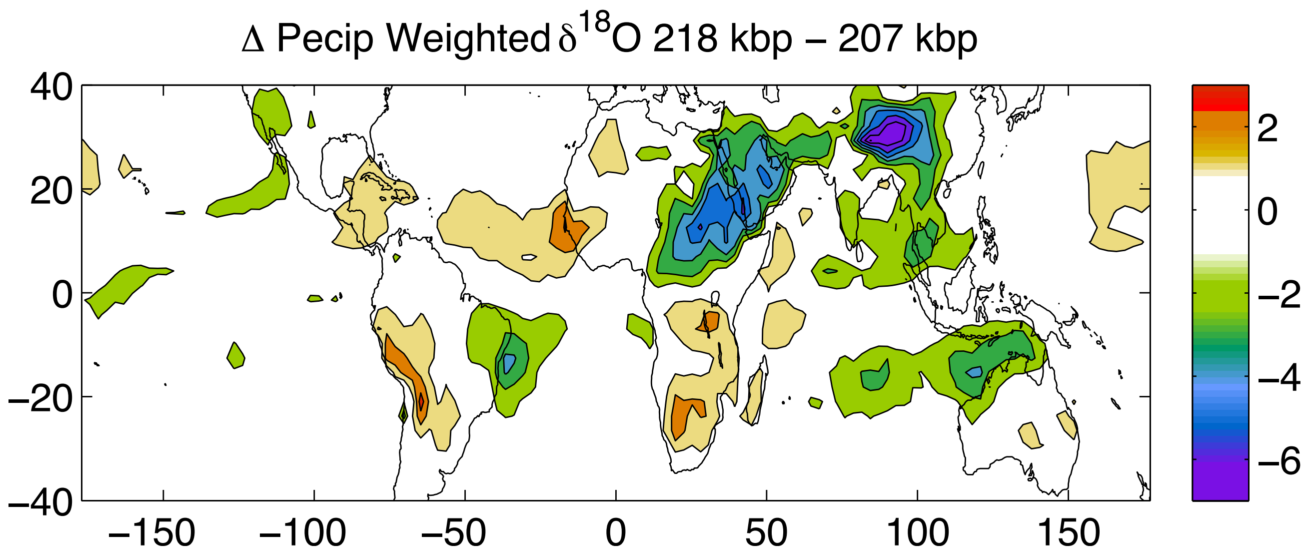

Figure 7. The difference the precipitation-weighted $\delta^{18}O$ ($\delta^{18}O_p$) associated with differences in insolation, 218 kbp minus 207 kbp. The contour interval is 1‰. Differences of less than 1 ‰ are colored white.

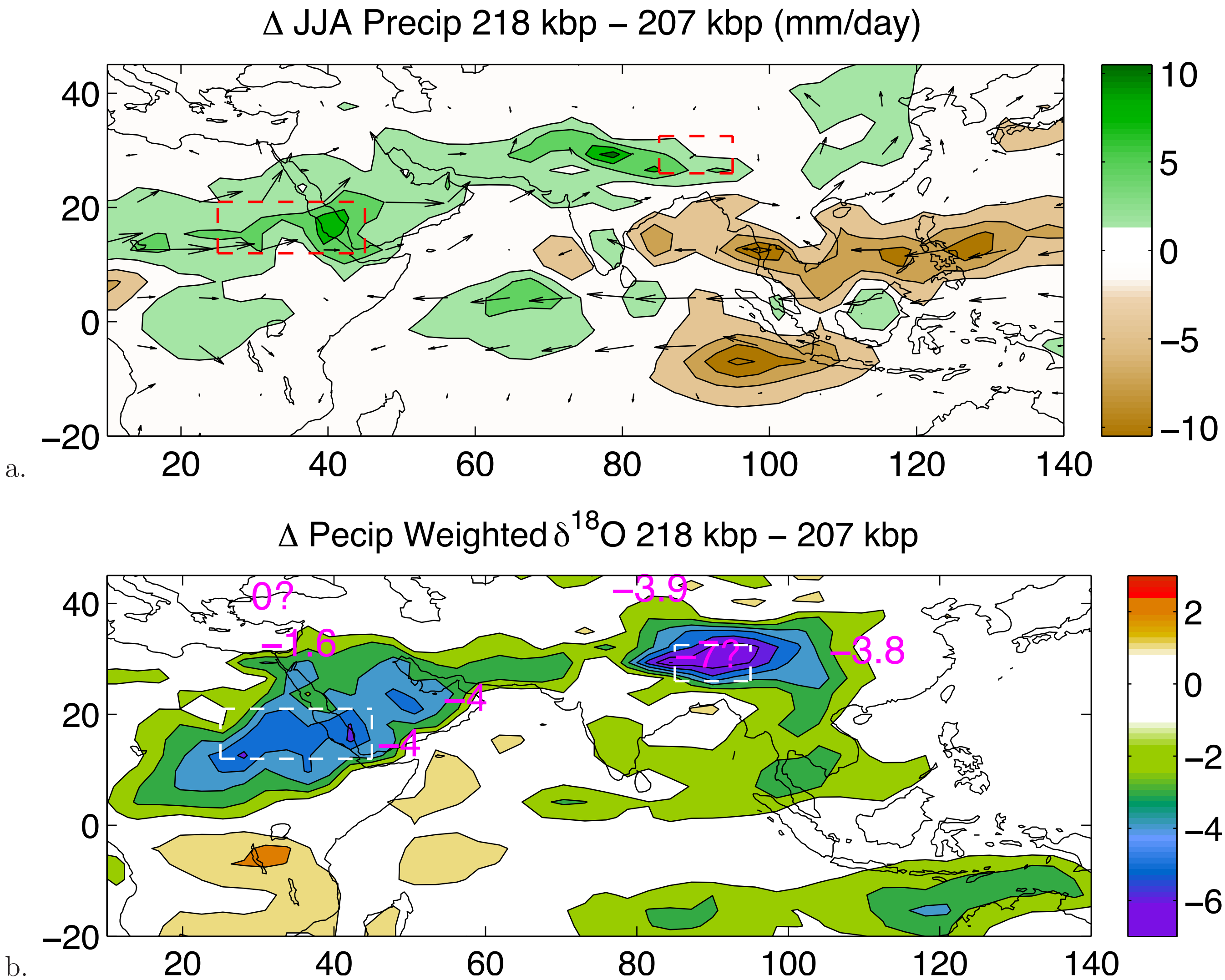

Figure 8. Regional excerpts of the differences in summer (JJA) (a) precipitation and (b) $\delta^{18}O_p$ associated with extremes in the insolation forcing, shown in Figures 5 and 7. Superposed on the JJA precipitation are the changes in the 850 hPa wind velocity; numbers in red in panel (b) indicate the scaled difference in $\delta^{18}O_c$ recorded in the stalagmites listed in Table 1, high-minus low- JJA insolation. The maximum vector length is 11.5 m/s. Contouring and coloring as in Figures 5(b) and 7. The red/white boxes indicate the regions used in the calculations of section 4.1 and shown in Table 2 and Figures 9 and 10.

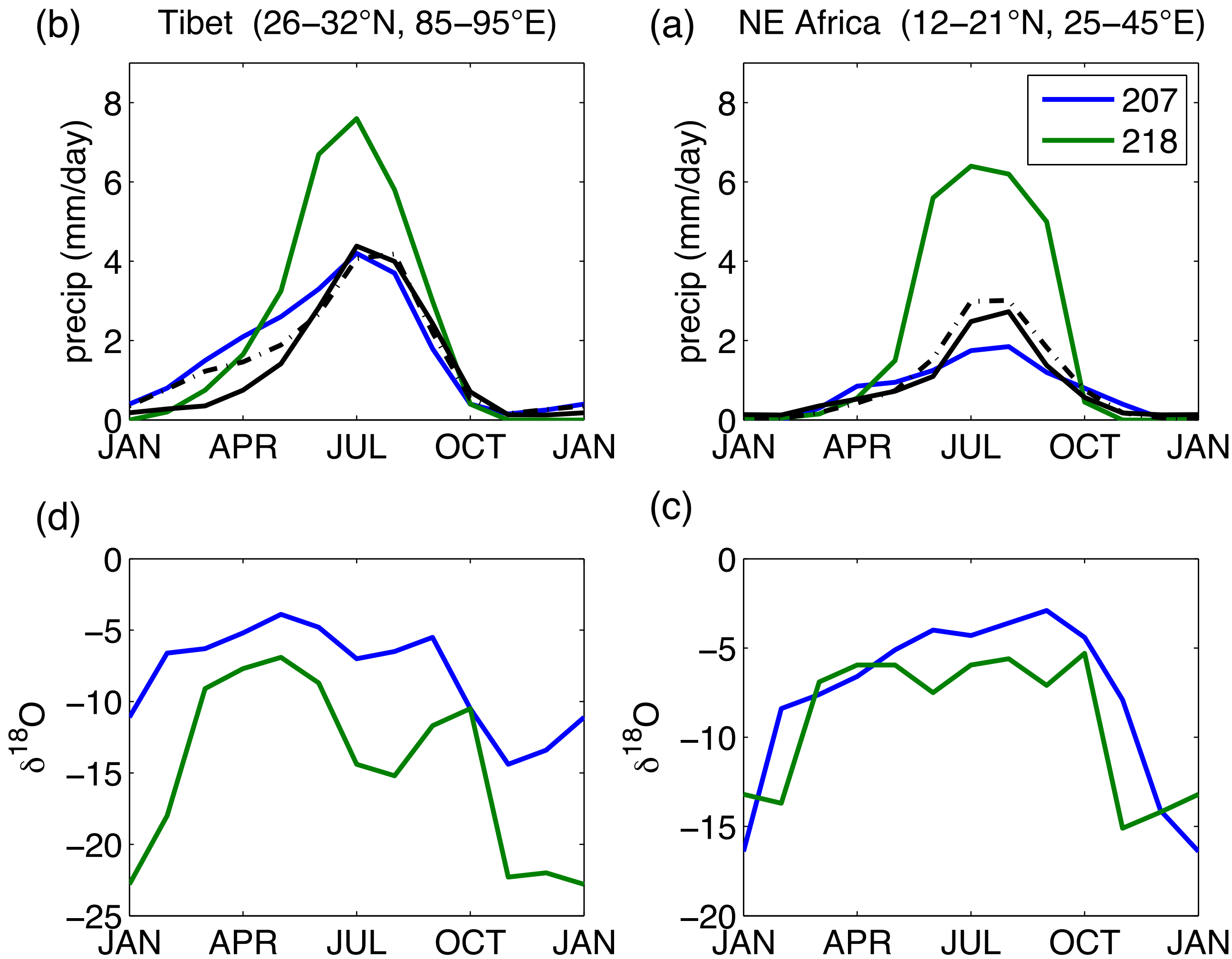

Figure 9. The climatological annual cycle of precipitation and the monthly $\delta^{18}O$ of precipitation averaged over Tibet and northeast Africa, the regions of maximum differences in summer precipitation and $\delta^{18}O_p$ associated with the extremes in the insolation forcing. Values in green (blue) are for 218 kbp (207 kbp) insolation, a time of maximum (minimum) summer insolation in the Northern Hemisphere. Also for reference is the annual cycle of precipitation from the control (Modern-Day) simulation of the climate model using modern-day insolation (solid black) and from observations (blacked dashed); the latter is from the NOAA Climate Prediction Center Merged Analysis of Precipitation (CMAP) product [*Xie and Arkin*, 1997]. Averages are taken over the boxed regions in Figure 8. The units on $\delta^{18}O$ are ‰.

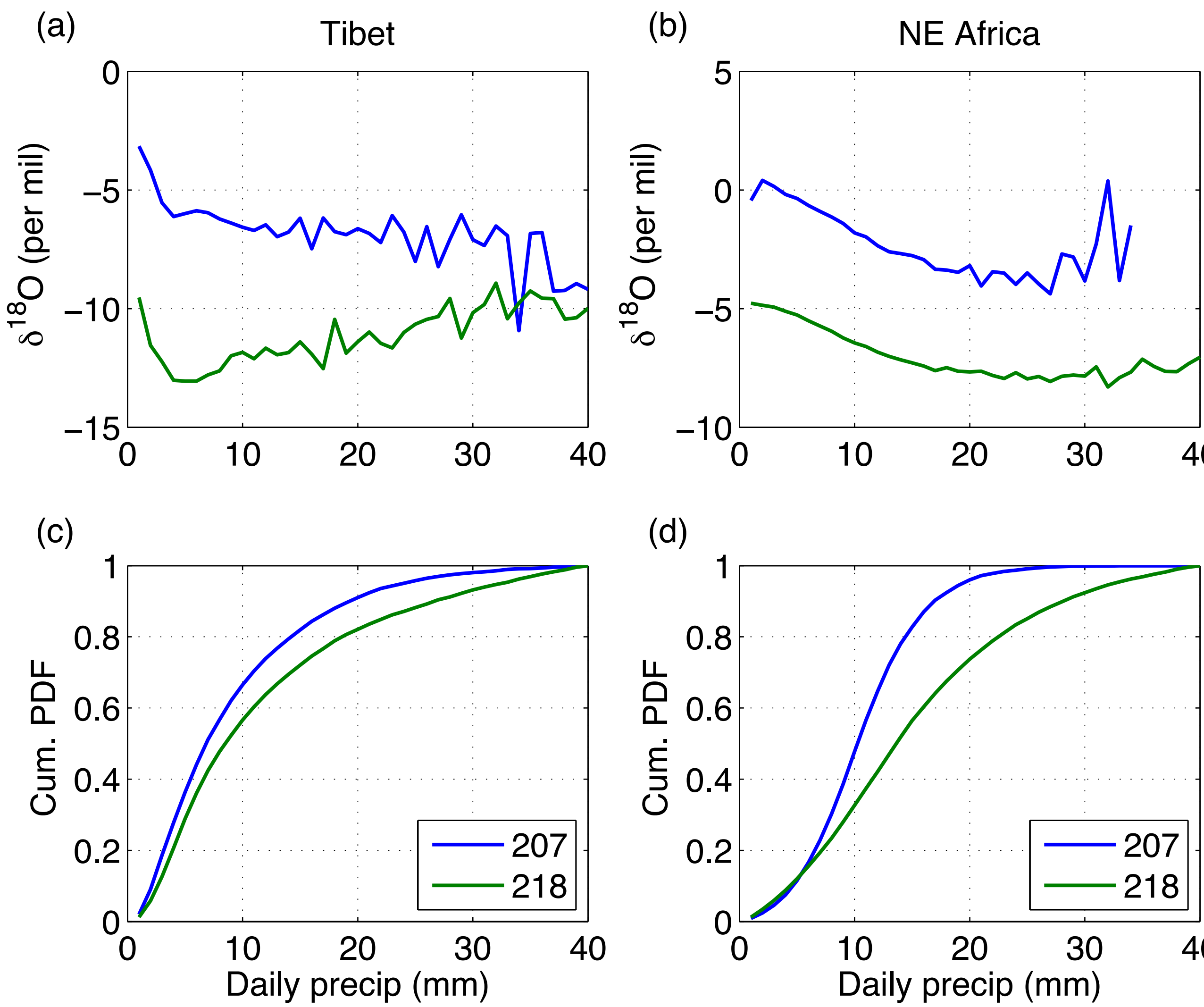

Figure 10. Top panels: the average $\delta^{18}O$ of the daily average precipitation in summer, binned as a function of the daily precipitation amount for (a) Tibet and (b) NE Africa. Bottom panels: the cumulative precipitation in summer for (c) Tibet and (d) NE Africa, binned by daily precipitation amount. For these calculations, we use 30 years of daily data from all of grid points within the regions indicated in Figure 8.

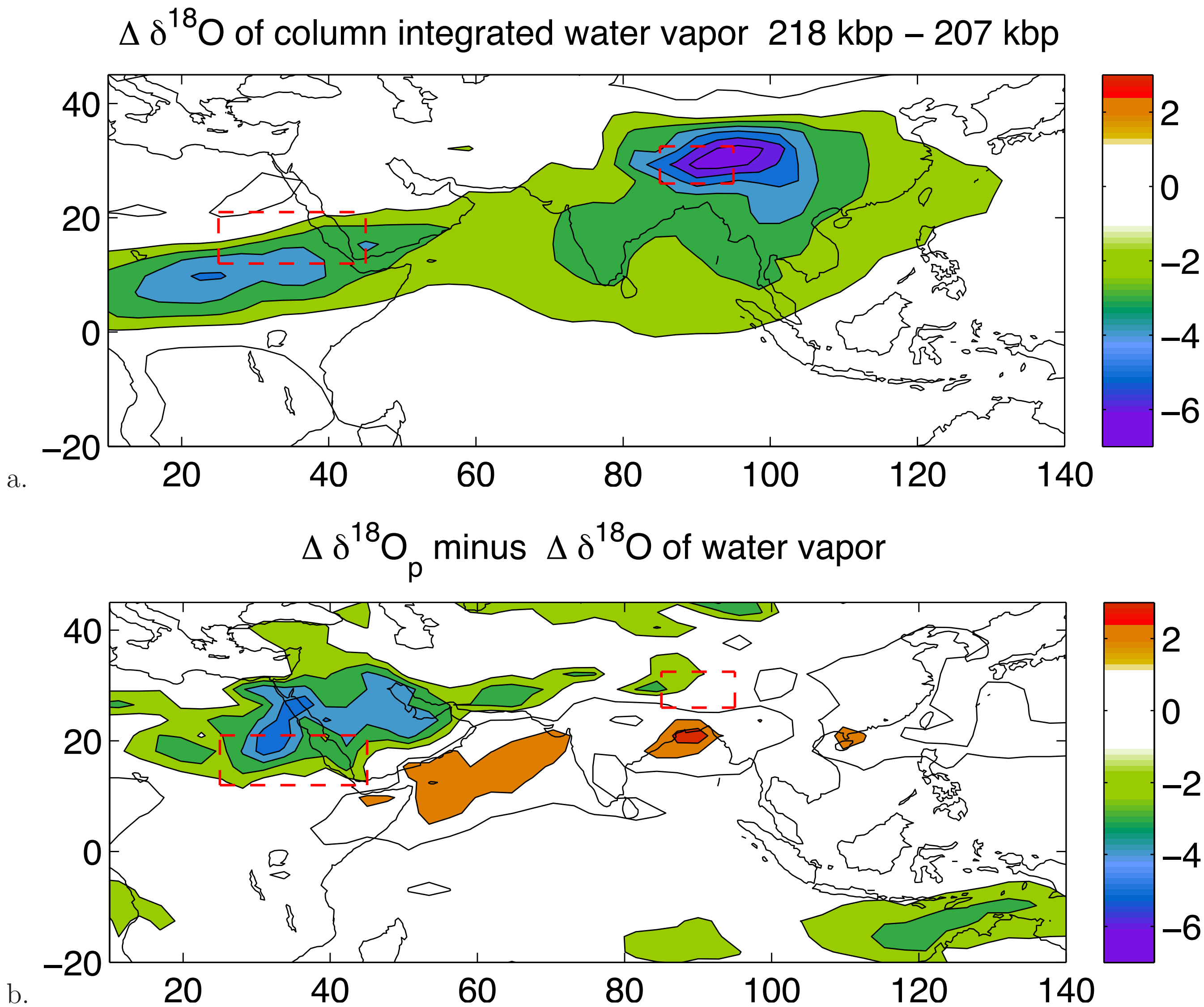

Figure 11. (a) The change in the $\delta^{18}O$ of the column integrated water vapor $\delta^{18}O_v$, high-insolation experiment minus low-insolation experiment. (b) The change in $\delta^{18}O_p$ that is not explained by the change in the $\delta^{18}O$ of the water vapor in the local environment: $(\delta^{18}O_p(218) - \delta^{18}O_p(207)) - (\delta^{18}O_v(218) - \delta^{18}O_v(207))$. Units are per mille; contour interval as in Figure 7.

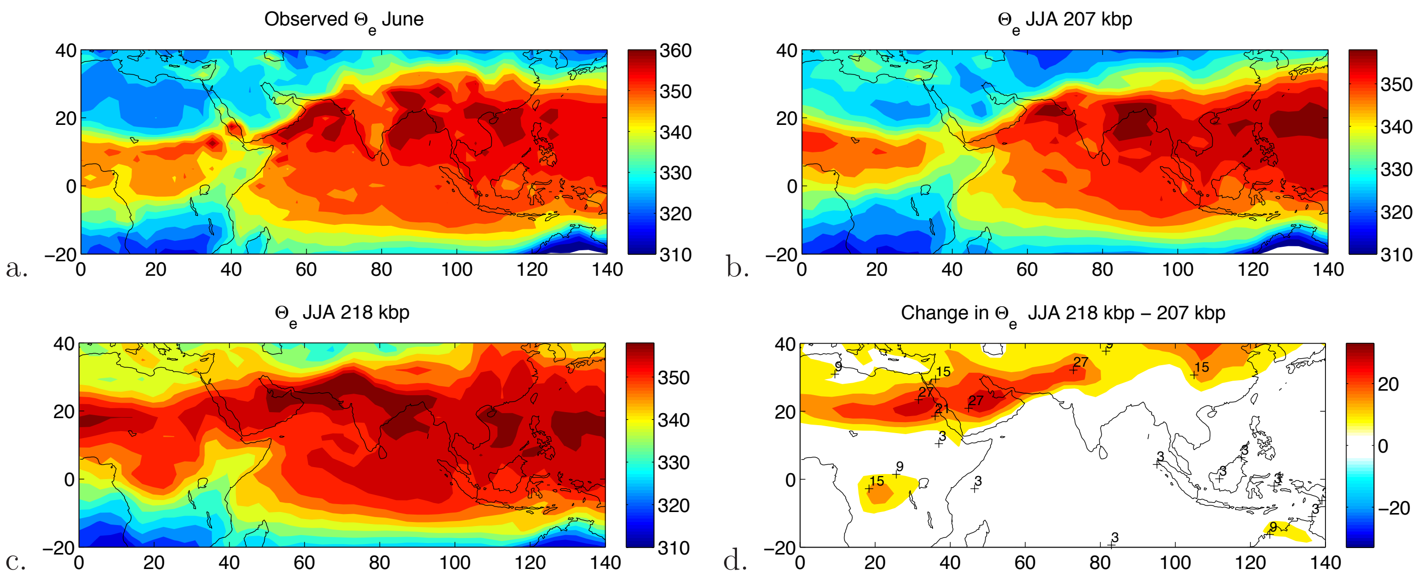

Figure 12. Near-surface equivalent potential temperature θ_e in (a) June at the onset of the monsoon from observations, and for summertime (JJA) in the (b) low-insolation experiment, and (c) high-insolation experiment. Panel (d) shows the difference between the high- and low-insolation experiments. Units are Kelvin. The observed θ_e is calculated from NCEP Reanalysis data provided by the NOAA/OAR/ESRL PSD, Boulder, Colorado, USA, from their Web site at http://www.esrl.noaa.gov/psd.

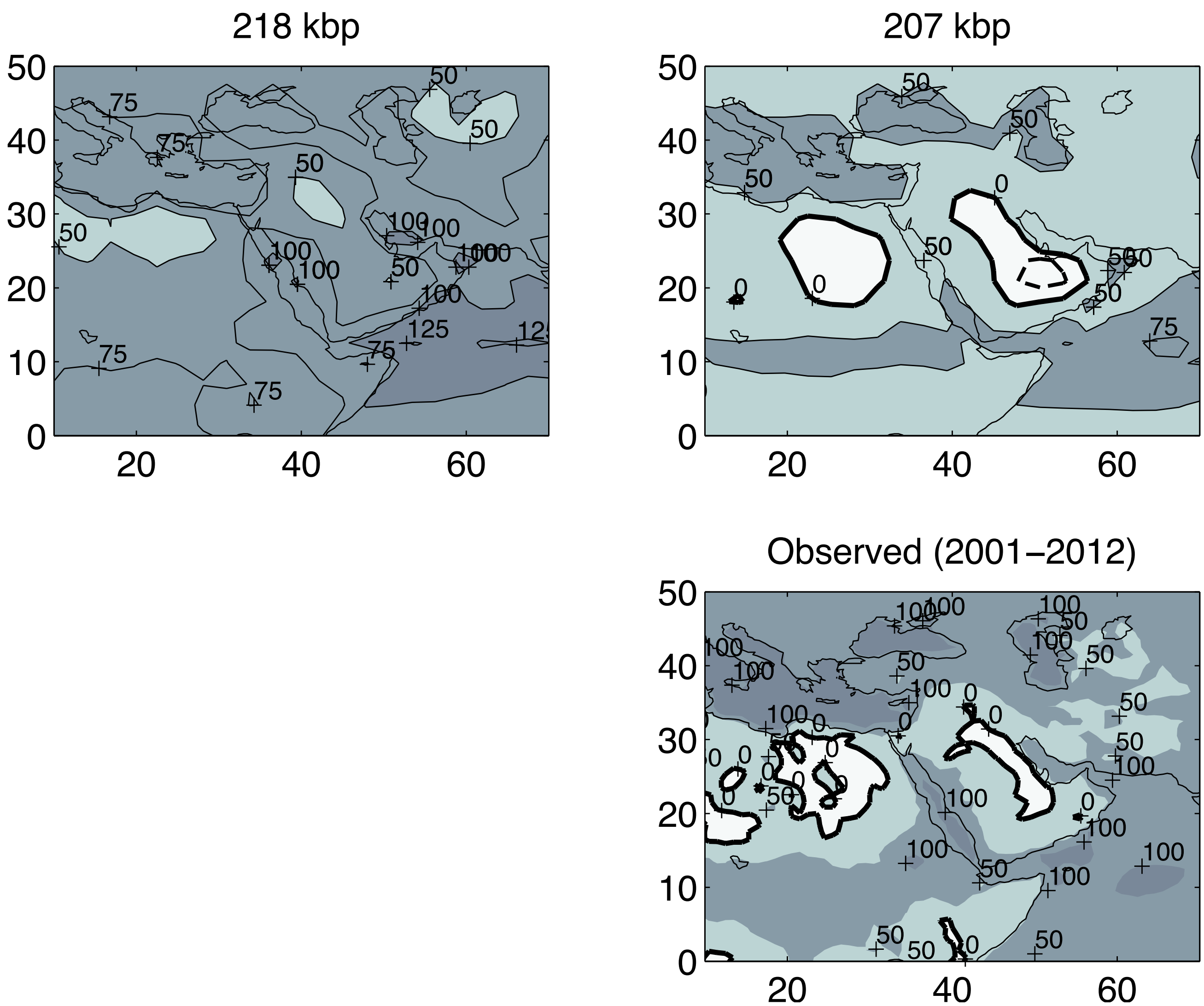

Figure 13. The net radiation at the top of the atmosphere for June-August from the (left) 218 kyr and (right) 207 kbp simulations; also shown is the observed net radiation from CERES (2001-2012). Contour interval is 25 Wm^{-2}; the bold (dashed) line is the zero (-25 Wm^{-2}) contour. Positive values indicate an energy gain by the atmosphere.

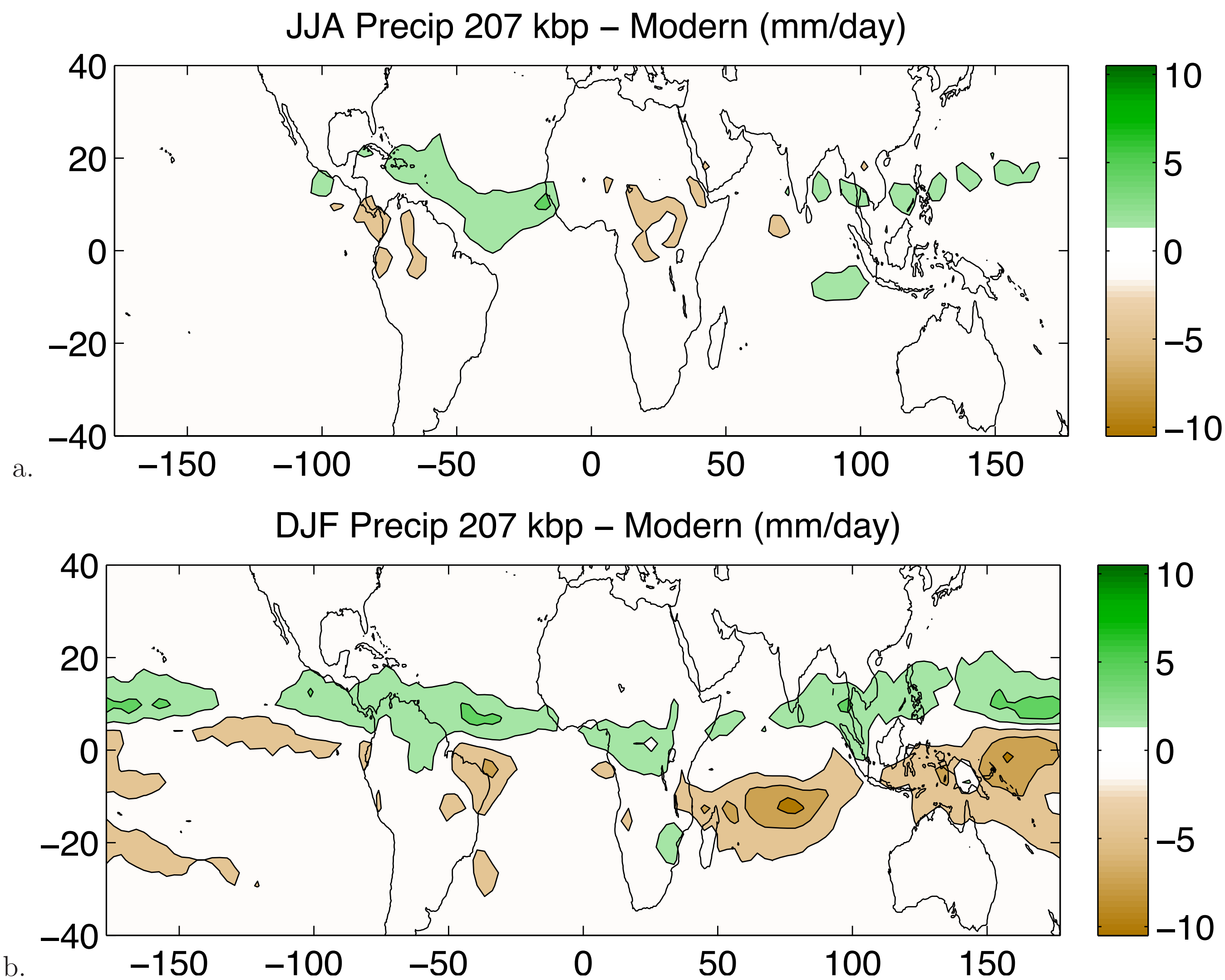

Figure A1. The difference between the climatological precipitation in the low-insolation (207 kbp) experiment minus the Modern-Day (i.e., with today's insolation) experiment: JJA (top) and DJF (bottom). The contour interval is 3 mm/day. Differences less than 1.5 mm/d are white.

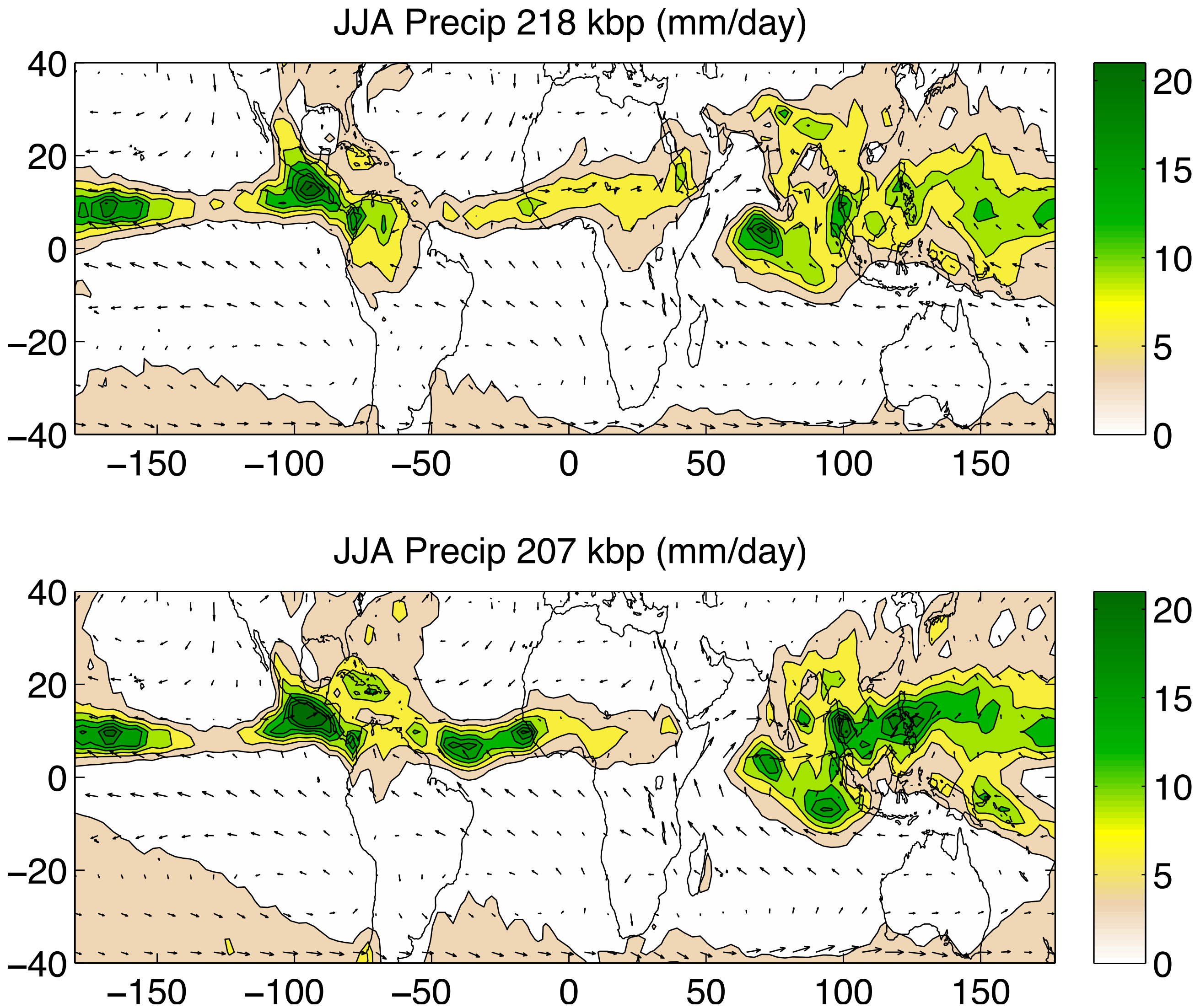

Figure A2. The climatological JJA precipitation and 850 hPa wind velocity from the (top) high-insolation (218 kbp) and (bottom) low-insolation (207 kbp) experiment. Contour interval is 3 mm/day. The maximum wind vector is 14.4 m/s.